

A new model for ionospheric total electron content: the impact of solar flux proxies and indices

Larisa P. Goncharenko¹, Cole A Tamburri², W. Kent Tobiska³, Samuel Schonfeld⁴, Phillip C Chamberlin⁵, Thomas N. Woods⁶, Leonid Didkovsky⁷, Anthea J Coster¹, and Shun-Rong Zhang⁸

¹Massachusetts Institute of Technology, Haystack Observatory

²University of Colorado

³Space Environment Technologies

⁴NASA

⁵University of Colorado, Laboratory for Atmospheric and Space Physics

⁶Laboratory for Atmospheric and Space Physics

⁷University of Southern California

⁸MIT Haystack Observatory

November 24, 2022

Abstract

We present a new high resolution empirical model for the ionospheric total electron content (TEC). TEC data are obtained from the global navigation satellite system (GNSS) receivers with a 1 x 1 spatial resolution and 5 minute temporal resolution. The linear regression model is developed at 45N, 0E for the years 2000 - 2019 with 30 minute temporal resolution, unprecedented for typical empirical ionospheric models. The model describes dependency of TEC on solar flux, season, geomagnetic activity, and local time. Parameters describing solar and geomagnetic activity are evaluated. In particular, several options for solar flux input to the model are compared, including the traditionally used 10.7cm solar radio flux (F10.7), the Mg II core-to-wing ratio, and formulations of the solar extreme ultraviolet flux (EUV). Ultimately, the extreme ultraviolet flux presented by the Flare Irradiance Spectral Model, integrated from 0.05 to 105.05 nm, best represents the solar flux input to the model. TEC time delays to this solar parameter on the order of several days as well as seasonal modulation of the solar flux terms are included. The Ap₃ index and its history are used to reflect the influence of geomagnetic activity. The root mean squared error of the model (relative to the mean TEC observed in the 30-min window) is 1.9539 TECu. A validation of this model for the first three months of 2020 shows excellent agreement with data. The new model shows significant improvement over the International Reference Ionosphere 2016 (IRI-2016) when the two are compared during 2008 and 2012.

A new model for ionospheric total electron content: the impact of solar flux proxies and indices

Larisa P Goncharenko¹, Cole A Tamburri^{1,2,3}, W Kent Tobiska⁴, Samuel J Schonfeld⁵, Phillip C Chamberlin⁶, Thomas N Woods⁶, Leonid Didkovsky⁷, Anthea J Coster¹, Shun-Rong Zhang¹

¹MIT Haystack Observatory, Westford, MA

²University of Colorado, Boulder, CO

³Boston College, Chestnut Hill, MA

⁴Space Environment Technologies, Pacific Palisades, CA

⁵Institute for Scientific Research, Boston College, Newton, MA

⁶University of Colorado, Laboratory for Atmospheric and Space Physics, Boulder, CO

⁷Space Sciences Center, University of Southern California

Key Points:

- The study introduces a formulation of new high-resolution empirical model for total electron content
- The impact of several solar flux proxies on the modeling of total electron content is examined
- The FISM2 EUV flux is found to perform the best, closely followed by $S_{10.7}$ index and the Mg II index

Corresponding author: Larisa P. Goncharenko, lpg@mit.edu

Corresponding author: Cole Tamburri, cole.tamburri@colorado.edu

20 **Abstract**

21 We present a new high resolution empirical model for the ionospheric total elec-
 22 tron content (TEC). TEC data are obtained from the global navigation satellite system
 23 (GNSS) receivers with a $1^\circ \times 1^\circ$ spatial resolution and 5 minute temporal resolution. The
 24 linear regression model is developed at 45° N, 0° E for the years 2000 - 2019 with 30 minute
 25 temporal resolution, unprecedented for typical empirical ionospheric models. The model
 26 describes dependency of TEC on solar flux, season, geomagnetic activity, and local time.
 27 Parameters describing solar and geomagnetic activity are evaluated. In particular, sev-
 28 eral options for solar flux input to the model are compared, including the traditionally
 29 used 10.7cm solar radio flux ($F_{10.7}$), the Mg II core-to-wing ratio, and formulations of
 30 the solar extreme ultraviolet flux (EUV). Ultimately, the extreme ultraviolet flux pre-
 31 sented by the Flare Irradiance Spectral Model, integrated from 0.05 to 105.05 nm, best
 32 represents the solar flux input to the model. TEC time delays to this solar parameter
 33 on the order of several days as well as seasonal modulation of the solar flux terms are
 34 included. The Ap_3 index and its history are used to reflect the influence of geomagnetic
 35 activity. The root mean squared error of the model (relative to the mean TEC observed
 36 in the 30-min window) is 1.9539 TECu. A validation of this model for the first three months
 37 of 2020 shows excellent agreement with data. The new model shows significant improve-
 38 ment over the International Reference Ionosphere 2016 (IRI-2016) when the two are com-
 39 pared during 2008 and 2012.

40 **1 Introduction**

41 Forecasting the future state of the ionosphere is a fundamental challenge for near-
 42 space environment research and operations. In pursuit of this goal, the international space
 43 weather community recognizes the need for enhanced fundamental understanding of space
 44 weather and its drivers and for improved predictive models of various ionospheric and
 45 thermospheric parameters. Recent efforts by the international Community Coordinated
 46 Modeling Center have identified several critical ionospheric and thermospheric param-
 47 eters that can be used for the assessment of the predictive capabilities (Scherliess et al.,
 48 2019). These parameters include total electron content (TEC), peak electron density ($N_m F_2$),
 49 and peak electron density height ($h_m F_2$). Reliable specification and forecasting of these
 50 parameters have significant societal impacts, as they can help mitigate uncertainties in
 51 precision timing and navigation, which impede space situational awareness, single-band
 52 high-frequency radio operations, and satellite geolocation. In particular, TEC is an im-
 53 portant parameter for estimation of phase delay effects in the ground-to-satellite nav-
 54 igation signals.

55 A significant ongoing effort to address these goals includes continuous development
 56 of different types of models, including first-principles models of the coupled ionosphere/thermosphere
 57 systems, data-assimilative models, and purely empirical models that are based on avail-
 58 able observations. Despite significant development and improvement in first-principles
 59 models, quantitative validation efforts indicate that empirical models often outperform
 60 first-principles models for geomagnetically quiet conditions, though first-principles mod-
 61 els can perform better during disturbed conditions if they include more complex and ac-
 62 curate input drivers (Shim et al., 2011, 2012, 2017b, 2018). Amongst the empirical mod-
 63 els, the International Reference Ionosphere (IRI) (Bilitza et al., 2017) and NeQuick (Nava
 64 et al., 2008) models are best known and most widely used. In particular, the IRI model
 65 is the basis for the International Standards Organization (ISO) International Standard
 66 IS 16457 (ISO16457, 2014).

67 Originally developed in the late 1960s, the IRI model has been continuously up-
 68 dated and improved as a result of coordinated dedicated efforts by the international re-
 69 search community. However, it still has certain limitations in simulating TEC. One of
 70 them is related to the representation of the electron density profile. The TEC in the IRI

71 model is obtained through integration of the electron density profile up to 2000 km and
 72 thus does not include contributions to TEC from the plasmasphere, which can reach sev-
 73 eral (2 - 6) TECu (1 TECu = 10^{16} el/m²) (Yizengaw et al., 2008; Cherniak et al., 2012;
 74 Shim et al., 2017a; L. Liu et al., 2018). In addition, the IRI model, as a global model,
 75 can significantly overestimate or underestimate regional TEC variations, even for mid-
 76 latitude locations (e.g. Zakharenkova et al. (2015)). As the IRI model electron density
 77 is based mostly on ionosonde observations below the F-region peak and on observations
 78 from Alouette 1,2 and ISIS 1,2 (Bilitza, 2004) above the F-region peak, deficiency in the
 79 description of the topside profile is thought to be the primary reason for the reported
 80 differences between IRI and TEC observations (Zakharenkova et al., 2015). The second
 81 limitation of IRI is related to its low sensitivity to short-term variations in solar ioniz-
 82 ing flux. As the model is aimed at representing monthly mean ionospheric conditions,
 83 it uses monthly values of either IG12 (a 12-month running mean of the global ionosphere
 84 index) or Rz12 (a 12-month running mean of the sunspot number) which F_{107} can be
 85 scaled to.

86 Recognition of the significant need for more accurate empirical models, together
 87 with the continued increase in availability and quality of ionospheric data, has led to a
 88 rapid development in additional empirical models during the last several years. Expan-
 89 sion of TEC data obtained from the GNSS satellites presented an opportunity to develop
 90 independent TEC models that do not rely on vertical extrapolation of the electron den-
 91 sity profile or assumptions about the shape of the profile above the peak electron den-
 92 sity, like in IRI or NeQuick. Such TEC models can be broadly characterized as global,
 93 regional, or local. Several global models were developed based on Global Ionospheric Maps
 94 (GIMs) which are generated since 1998 with 2-hour temporal resolution (Mannucci et
 95 al., 1998; Vergados et al., 2016; Komjathy et al., 2005). Mukhtarov et al. (2013a) has
 96 built a monthly mean TEC model with $5^\circ \times 5^\circ$ degree resolution in latitude and longi-
 97 tude utilizing data from the Center for Orbit Determination of Europe (CODE) and rep-
 98 resenting TEC variations as a function of solar flux, rate of change in solar flux, season,
 99 time of day, and magnetic latitude; further development of that model included depen-
 100 dence on geomagnetic activity (Mukhtarov et al., 2013b). Aa et al. (2012) developed a
 101 global TEC model based on GIMs provided by the Jet Propulsion Laboratory (JPL) and
 102 using empirical orthogonal function (EOF) analysis, a technique which decomposes data
 103 using functions determined by the data themselves rather than the predefined functions
 104 used in other methods such as Fourier decomposition (Chen et al., 2015). Lean et al. (2016)
 105 constructed a model of 2-hourly TEC data by combining representations of solar EUV,
 106 sinusoidal parameterizations of annual, semiannual, terannual, and biennial oscillations,
 107 diurnal, semidiurnal, and terdiurnal cycles, and geomagnetic activity. The distinctive fea-
 108 ture of the Lean et al. (2016) model is the description of solar ionizing flux; it includes
 109 total EUV irradiance summarized for wavelengths less than 105 nm and 11 time lags rang-
 110 ing from 0 and 12 hours to 36 days. Recognizing the limitations of IGS TEC GIM maps
 111 and their lower accuracy over the oceans, Feng et al. (2019) suggested a global TERM-
 112 GRID model that consists of 5183 independent single point empirical models.

113 Many new TEC empirical models were developed for the description of the regional
 114 ionosphere, including, for example, the ionosphere over Europe (Jakowski et al., 2011),
 115 China (Mao et al., 2008), North America (Chen et al., 2015), South Africa (Habarulema
 116 et al., 2010, 2011), Australia (Bouya et al., 2010), and the Arctic (J. Liu et al., 2014).
 117 Regional empirical models often outperform global empirical models as they are based
 118 on additional data not included in IGS GIM maps and use fewer assumptions about spa-
 119 tial variations in TEC. Single-location empirical models are often used to describe dis-
 120 tinctive ionospheric features over a specific geographic location and/or explore different
 121 modeling approaches (Mao et al., 2005; J. Liu et al., 2012; Huang & Yuan, 2014). Em-
 122 pirical ionospheric modeling remains an active area of research, as increasingly accurate
 123 and detailed global specification of the near-Earth space environment is required to fur-
 124 ther understand its intricate organization and behavior.

125 Ionospheric electron density is produced by solar EUV radiation at wavelengths less
 126 than 103 nm (Schunk and Nagy, 2009) that ionizes thermospheric atomic oxygen and
 127 molecular nitrogen and oxygen. The most important contribution to ionization comes
 128 from EUV radiation at wavelengths 26-34 nm which is mostly absorbed by atomic oxy-
 129 gen at altitudes above 200 km (Richards et al., 1994; Schunk & Nagy, 2009). Solar EUV
 130 flux is also an important source of atmospheric heating, determining neutral tempera-
 131 ture, composition and winds which are all directly coupled to the ionospheric photo-ionization,
 132 chemistry, and dynamics. Previous studies have demonstrated that solar EUV emission
 133 can be well described by the solar activity proxy $F_{10.7}$ which represents solar radio flux
 134 at the wavelength of 10.7 cm. We use the definitions of solar index and solar proxy from
 135 IS 21348 where a solar proxy is a data type used as a substitute for solar spectral irra-
 136 diances at other wavelengths or bandpasses and a solar index is a data type that is an
 137 activity level indicator. The vast majority of empirical ionospheric models, even those
 138 developed most recently, use the $F_{10.7}$ proxy to describe solar EUV influence on iono-
 139 spheric parameters (Mukhtarov et al., 2013a, 2013b; Chen et al., 2015; Themens et al.,
 140 2017; Feng et al., 2019; Zhang et al., 2005). The popularity of the $F_{10.7}$ proxy is based
 141 on its long data record, as it is available since 1947, and well-demonstrated performance
 142 for the description of critical frequency f_oF_2 (or peak electron density N_mF_2) that was
 143 historically widely available due to the abundance of ionosondes (L. Liu et al., 2006). How-
 144 ever, the $F_{10.7}$ proxy does not directly describe the solar emission in the EUV wavelength
 145 range < 102.5 nm which is directly responsible for the ionization of the thermosphere.
 146 In addition, as a significant portion of the contribution to TEC comes from the profile
 147 of electron density above the peak, and the impact of different portions of the EUV spec-
 148 trum varies with altitude, it is not immediately clear if the $F_{10.7}$ proxy performs as well
 149 for TEC as for f_oF_2 . With increasing availability of satellite EUV data, numerous ob-
 150 servational datasets and new indices became available within the last two decades that
 151 can better characterize solar energy input to the thermosphere. These observations in-
 152 clude solar extreme ultraviolet monitor (SEM) onboard the Solar and Heliospheric Ob-
 153 servatory (SOHO), Solar Backscatter Ultraviolet (SBUV) spectrometer on NOAA satel-
 154 lites (Viereck et al., 2001), and SEE onboard TIMED (T. Woods et al., 2000; T. N. Woods,
 155 2005). New indices include, for example, the $S_{10.7}$ index that reflects integrated solar emis-
 156 sion between 26 - 34 nm (W. K. Tobiska et al., 2008; B. Bowman et al., 2008a), the Mg
 157 II core-to-wing ratio that corresponds to emission near 160 nm (Viereck et al., 2001; B. Bow-
 158 man et al., 2008a), the $M_{10.7}$ index which is derived from the Mg II (W. K. Tobiska et
 159 al., 2008; B. Bowman et al., 2008a), the X_{b10} index that corresponds to 0.1-0.8 nm so-
 160 lar X-ray emission (W. Tobiska & Bouwer, 2005), and the $Y_{10.7}$ index that combines X_{b10}
 161 and Lyman-alpha emission. The impact of these indices is better studied in the thermo-
 162 sphere, and their usage substantially improved thermospheric density models (W. K. To-
 163 biska et al., 2008; B. Bowman et al., 2008a; Emmert et al., 2008; He et al., 2018). How-
 164 ever, the impact of these indices on improvement in ionospheric empirical models and,
 165 specifically, on TEC, is much less known. Maruyama (2010) compared the performance
 166 of models that include the sunspot number R, solar $F_{10.7}$ proxy, Mg II index or $S_{10.7}$ in-
 167 dex on mid-latitude TEC over Japan and concluded that the $S_{10.7}$ index was the best
 168 proxy for modeling TEC of those included in the study. Lean et al. (2011) used TIMED
 169 SEE observations with the $F_{10.7}$ proxy and the Mg II index to develop a model of EUV
 170 variability and later use it in the global TEC model (Lean et al., 2016; Lean, 2019). It
 171 is thus of great interest to further examine whether new solar flux indices are better suited
 172 for empirical models of TEC than the $F_{10.7}$ proxy.

173 Another issue with the $F_{10.7}$ proxy relates to its ability to describe both the direct
 174 impact on ionospheric electron density (through ionization processes) and indirect im-
 175 pact (through thermospheric heating that operates on longer temporal scales). The re-
 176 sponse of electron density to an increase in $F_{10.7}$ saturates for high levels of solar activ-
 177 ity, usually between 160 and 200 sfu ($1 \text{ sfu} = 10^{-22} \text{ W m}^{-2} \text{ Hz}^{-1}$), depending on latitude
 178 (Lei et al., 2005; L. Liu et al., 2006). To account for this saturation, various ionospheric
 179 models usually use a combination of the $F_{10.7}$ flux and the 81-day average of $F_{10.7}$ flux

180 (Richards et al., 1994; L. Liu et al., 2006; Brum et al., 2011). While it might be suffi-
 181 cient for some types of studies, the need to rely on the knowledge of solar flux that will
 182 occur up to 40 days in the future is not acceptable for ionospheric predictions. Maruyama
 183 (2010) investigated the delayed response of TEC to several solar flux proxies and con-
 184 cluded that inclusion of 1-2 day delays, the 27-day delay, and the 81-day delay improved
 185 TEC modeling. The 2-day delay in the neutral atmosphere, especially in the tempera-
 186 ture (Zhang et al., 2015), is a very pronounced feature that has been well recognized and
 187 included in the MSIS models. Lean et al. (2016) found that adding several lagged terms
 188 with 1-36 day delays of daily solar EUV irradiance alleviates the need for 81-day aver-
 189 aging of solar flux. Thus, the concept of using delayed solar flux terms instead of the 81-
 190 day average term has been already introduced and demonstrated.

191 This paper describes a first phase in a new empirical TEC model that has several
 192 distinct features as compared to already available models. It uses TEC data from the
 193 CEDAR Madrigal database that are obtained with much higher resolution in space and
 194 time as compared to GIM TEC. Recognizing that representation of diurnal behavior with
 195 superposition of harmonics with a 24-hr period, 12-hr period, etc., results in an inad-
 196 equate description of diurnal behavior, especially around sunrise and sunset, the proposed
 197 model is based on independent fitting of TEC with 30-min temporal resolution. As a main
 198 portion of the current effort, we examine different representations of the solar ionizing
 199 flux in order to determine the solar flux proxy most suitable for TEC. In addition, the
 200 model considers the delayed response of TEC to solar ionization. In this study, the pro-
 201 posed model and solar flux proxies are examined for a single mid-latitude location, 45°N
 202 and 0°E. Future efforts will present extension of this approach to other locations.

203 **2 Data Sources and Preparation**

204 **2.1 CEDAR Madrigal Database**

205 In this new empirical model, we use the CEDAR Madrigal database for TEC ob-
 206 servations that were processed, and provided for public access, by the Massachusetts In-
 207 stitute of Technology’s Haystack Observatory (Rideout & Coster, 2006; Vierinen et al.,
 208 2016). This database includes ionospheric observations from an ever increasing set of glob-
 209 ally distributed GNSS dual-frequency ground-based receivers, beginning with 500 re-
 210 ceivers in 2000 to more than 6000 in 2020. By including data from all publicly available
 211 multi-frequency GNSS receivers, and by providing data products at a high cadence (5
 212 min) and high spatial resolution (1 deg latitude and longitude), the Madrigal standard
 213 vertical TEC product provides a more comprehensive and detailed description of TEC
 214 variations than the GIM TEC product. GIM TEC products are based on only the sever-
 215 al hundred IGS receivers, and are available at a 2 hour cadence in a bin of 5 degrees
 216 latitude and longitude. The procedure used in the Madrigal processing to calculate the
 217 unknown satellite and receiver biases is provided in Vierinen et al. (2016). Although not
 218 used here, a new higher resolution TEC product is also available in Madrigal that in-
 219 cludes all of the line-of-sight TEC at 1 min resolution. The standard Madrigal TEC prod-
 220 uct is available in the CEDAR Madrigal database from January 1, 2000. The empirical
 221 model discussed in this study is based on 20 years of TEC data, from January 1, 2000
 222 to December 31, 2019, almost two solar cycles of data. This large dataset is well suited
 223 for empirical modeling, as it provides good coverage of both solar minimum and solar
 224 maximum conditions, and contains a large number of geomagnetic storms.

225 **2.2 Data Preparation and Error Reduction**

226 Techniques for error and noise reduction in these data are employed nevertheless.
 227 The data are of varying quality, with clear outliers present at times. For example, from
 228 -33° longitude to -27° longitude, data is scarce. In addition to the incongruous complete-
 229 ness of the data set, small artificial variations in TEC track the motion of satellites ac-

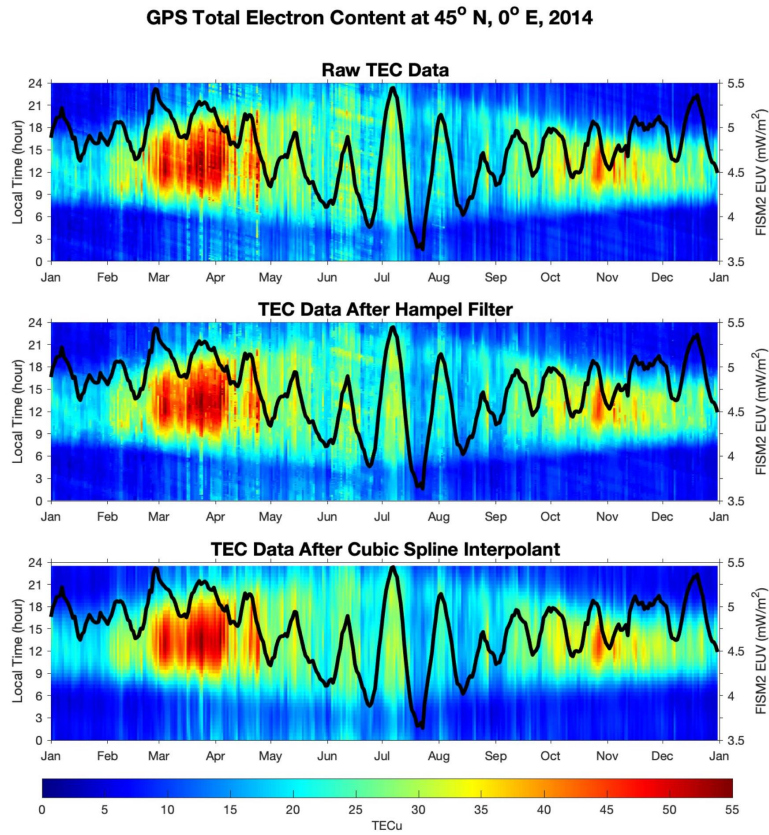


Figure 1. An example of the data cleaning process for the year 2014 at 45°N, 0°E. The solar flux proxy used in the model is shown as a black line to indicate the correlation between increases in solar flux and TEC. Periodic fluctuations in TEC and solar flux also occur in concert.

230 cording to sidereal hour rather than universal time (UT) hour. These variations are roughly
 231 the same magnitude as small-scale fluctuations in TEC which the model ideally reflects.
 232 It is therefore important to minimize or remove the error due to this sidereal motion prior
 233 to model construction.

234 To account for the first issue in data quality (the presence of outliers), a Hampel
 235 filter is applied with a 13-point window and a 1-standard-deviation criterion for outlier
 236 detection. If a given point varies from the median of 13 surrounding data points by 1
 237 standard deviation, the datum is replaced with the median of the 13-point window. A
 238 similar filter is then applied, ordering the data from day-to-day rather than hour-to-hour,
 239 with a 3-day window around each point and a 3-standard-deviation criterion for outlier
 240 replacement. After the application of this filter, in order to account for the sidereal mo-
 241 tion of satellites, a cubic spline interpolant is applied to the data with a low tolerance
 242 for outlier removal. Figure 1 shows the result of this process for the year 2014 at 45°N,
 243 0°E.

244 **2.3 Solar Flux Proxies**

245 One of the goals of this study is to compare the impact of different solar flux for-
 246 mulations on the performance of the new empirical TEC model. We examined 11 solar
 247 flux formulations that include direct EUV measurements, proxies that are measured di-
 248 rectly ($F_{10.7}$, Mg II core-to-wing ratio, Lyman-alpha), proxies that are special cases of
 249 measurements ($S_{10.7}$, corrected $F_{10.7}$, $P_{10.7}$) and finally the proxies from solar irradi-
 250 ance models (SIP $E_{10.7}$, FISM2 EUV). This section presents several recently developed
 251 proxies that were not yet applied to an ionospheric model and compares them to prox-
 252 ies traditionally used in studying the solar influence on the upper atmosphere. The uti-
 253 lized solar flux data over the course of 2000 - 2019 (time period used in model develop-
 254 ment) are shown in Figure 2.

255 **2.3.1 TIMED SEE EUV**

256 The Thermosphere Ionosphere Mesosphere Energetics Dynamics (TIMED) space-
 257 craft includes the Solar EUV Experiment (SEE) as one of its four scientific instruments
 258 (T. N. Woods, 2005). The data is available from the University of Colorado at Boulder
 259 Laboratory for Atmospheric and Space Physics (LASP) website ([http://lasp.colorado](http://lasp.colorado.edu/home/see/data/)
 260 [.edu/home/see/data/](http://lasp.colorado.edu/home/see/data/)), and an overview of the data for 2000 - 2019 is shown in Fig-
 261 ure 2(a). Flux measurements are provided for each nanometer in the EUV range; for this
 262 study, the data were processed by integrating from 0.5 to 105 nanometers. There are note-
 263 worthy omissions in the TIMED SEE EUV data which prompt evaluation of other datasets
 264 describing variation in the EUV range. These include (i) that the TIMED mission was
 265 launched in 2002, two years after the commencement of the TEC data collected by the
 266 Madrigal database, and (ii) that there exist several data gaps, typically associated with
 267 the TIMED “safe mode,” within the 2002-2019 tenure of the data. These result in a sig-
 268 nificant lack of data around the maximum of solar cycle 23.

269 **2.3.2 SOHO SEM EUV**

270 The Solar and Heliospheric Observatory (SOHO) spacecraft includes the Solar EUV
 271 Monitor (SEM), the data for which are made available by USC Dornsife ([https://dornsifecms](https://dornsifecms.usc.edu/space-sciences-center/download-sem-data/)
 272 [.usc.edu/space-sciences-center/download-sem-data/](https://dornsifecms.usc.edu/space-sciences-center/download-sem-data/)) and are shown for the rel-
 273 evant time period in Figure 2(b). These data provide the 0.1 - 50 nanometer flux as a
 274 daily average value, normalized to 1 astronomical unit (AU). Although a smaller wave-
 275 length range than the TIMED SEE data, it includes the 26 - 34 nanometer bandwidth
 276 which is considered the primary driver of ionization in the F-region ionosphere. There-
 277 fore, this dataset is considered valuable despite its omission of radiation in the 50 - 105
 278 nanometer range included in other EUV data. The data are available with a 15 second

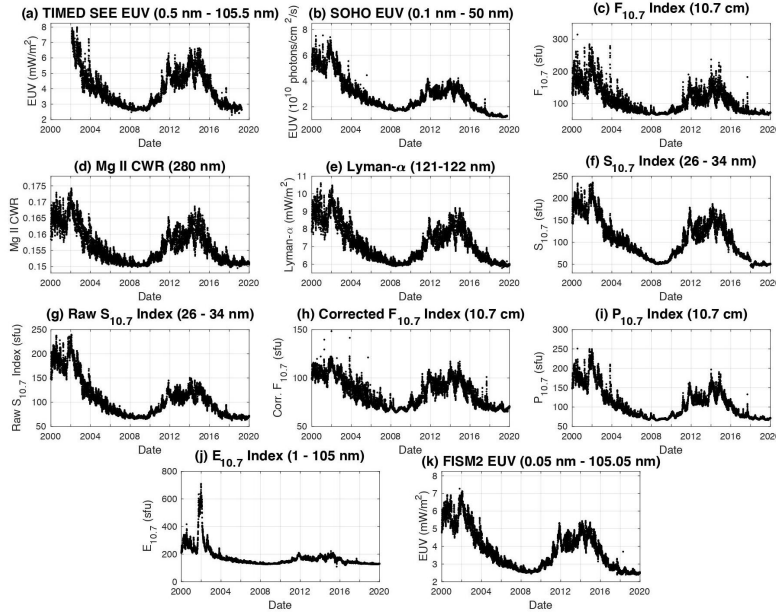


Figure 2. Time series comparison of the solar flux proxies studied for the period over which the model is built. Only the TIMED SEE EUV data do not cover the entirety of the 2000 to 2019 period, having commenced in 2002.

279 cadence for 2018 and 2019 and a daily average for 1996 through 2019. The latter are used
 280 for the present modeling purposes.

281 **2.3.3 $F_{10.7}$**

282 Past empirical models for ionospheric TEC have typically used the 10.7 centime-
 283 ter radio flux density ($F_{10.7}$) as the input proxy for solar flux. This is partially due to
 284 the temporal coverage provided by the $F_{10.7}$ dataset. Developed first in 1947, this proxy
 285 provides a data source for solar variability across several solar cycles. It is mostly the
 286 extreme ultraviolet (EUV) wavelengths - roughly the 26 to 34 nanometer bandwidth in
 287 particular - which directly ionize the F-region ionosphere and are therefore absorbed be-
 288 fore reaching the ground. While it does not directly contribute to ionization or atmo-
 289 spheric heating, $F_{10.7}$ has been shown to correlate with satellite acceleration (Jacchia,
 1959) and EUV variability over multi-year time scales (Lean et al., 2011).

291 Data for $F_{10.7}$ are available for more than six solar cycles. The data used here are
 292 provided by the CEDAR Madrigal database and shown in Figure 2(c). It should be noted
 293 that $F_{10.7}$ is a daily value measured between 17-20 UT. In ionospheric TEC models, the
 294 index is typically applied in conjunction with an 81-day moving average, which takes the
 295 mean of $F_{10.7}$ values 40 days prior to and following the day in question (F_{81}). The In-
 296 ternational Reference Ionosphere (IRI) model depends on sunspot number (Rz12) and
 297 an ionosphere-effective solar index (IG12), and includes both the daily $F_{10.7}$ and F_{81} as
 298 solar flux and ionospheric inputs. Feng et al. (2019) use an average of these two indices
 299 as their solar flux input parameter. Mukhtarov et al. (2013b) use the daily $F_{10.7}$ and the
 300 linear rate of change of $F_{10.7}$, K_F .

301 **2.3.4 Mg II Core-to-Wing ratio**

302 The Mg II index is the core-to-wing ratio of the Mg II Fraunhofer doublet centered
 303 at 280 nanometers (Heath & Schlesinger, 1986). The k and h emission lines at 279.55
 304 and 280.27 nanometers are generated in the upper chromosphere, with nearby wings (“back-
 305 ground”) generated in the upper photosphere. Calculation of the ratio between these emis-
 306 sion lines and nearby wings provides a measure for chromospheric activity which is of-
 307 ten used as a proxy for the extreme ultraviolet flux. The data, the relevant subset of which
 308 are shown in Figure 2(d), are available since 1978 and are developed as a composite in-
 309 dex from several data sources (<http://www.iup.uni-bremen.de/UVSAT/Datasets/mgii>),
 310 including the Global Ozone Monitoring Experiment (GOME), Scanning Imaging Absorp-
 311 tion Spectrometer for Atmospheric Chartography (SCIAMACHY), GOME-2A, GOME-
 312 2B, and GOME-2C missions. These data are updated daily. Viereck et al. (2001) sug-
 313 gested for the period of 1978 through 2000 that the Mg II core-to-wing ratio serves as
 314 a better proxy for EUV radiation in the region of most concern to the ionosphere (roughly
 315 26 to 34 nanometer wavelengths) than the $F_{10.7}$ index. Its performance in representing
 316 the radiation corresponding to this wavelength range makes it particularly applicable to
 317 the study at hand.

318 **2.3.5 Lyman-Alpha Index**

319 Machol et al. (2019) describes the development of the Lyman-alpha (Lyman- α) com-
 320 posite. This represents the solar output at 121.56 nm, the strongest solar vacuum ultra-
 321 violet emission line. The data are available from the LASP Interactive Solar Irradiance
 322 Data Center (<http://lasp.colorado.edu/lisird/>), and the corresponding time se-
 323 ries for 2000 - 2019 is shown in Figure 2(e). The time series takes into account measure-
 324 ments from several instruments and models, as listed on the LASP Interactive Solar Ir-
 325 radiance Data Center webpage corresponding to the dataset. Machol et al. (2019) de-
 326 scribe the scaling of the values from each dataset to match the SORCE SOLSTICE re-
 327 ference levels at 1 astronomical unit (AU).

328 **2.3.6 Jacchia-Bowman 2008 (JB2008) $S_{10.7}$ index**

329 W. K. Tobiska et al. (2008) and ISO14222 (2013) describe the development of the
 330 $S_{10.7}$ index, a solar flux proxy measured by the SOHO Solar Extreme-ultraviolet Mon-
 331 itor (SEM), the TIMED SEE, the SDO EVE, the GOES-14,-15 EUVS, and the GOES-
 332 16,-17 EXIS. It isolates the 26 - 34 nanometer range, the bandwidth which has the most
 333 physical impact on ionization in the F-region ionosphere (Banks & Kockarts, 1973). The
 334 daily values are available for download at the Jacchia-Bowman 2008 Empirical Thermo-
 335 spheric Density Model (JB2008) website (<https://sol.spacenvironment.net/JB2008/>).
 336 The 2000 - 2019 time series is shown in Figure 2(f). The data are available since 16 De-
 337 cember 1995 and are updated daily. The relationship between the $F_{10.7}$ and $S_{10.7}$ indices
 338 is shown in the middle panel of Figure 3. The best-fitting function between the two in-
 339 dices is quartic after scaling $S_{10.7}$ to the units of $F_{10.7}$. It is notable that the relation-
 340 ship between the two is not linear, though directly proportional.

341 In addition to the $S_{10.7}$ index, which is modified to remove energy at the top of the
 342 atmosphere during solar minimum as a method of compensating for thermospheric cool-
 343 ing at the bottom of the thermosphere, a pure solar version of this index, also called raw
 344 without the energy removal, is tested. The corresponding time series is shown in Fig-
 345 ure 2(g). It is found that the official $S_{10.7}$ index, described above, yields a better-performing
 346 ionospheric TEC model. These results are discussed below.

347 **2.3.7 Corrected $F_{10.7}$**

348 Seeking to correct for some discrepancy observed between $F_{10.7}$ and EUV, Schonfeld
 349 et al. (2019) present a corrected $F_{10.7}$ index by decomposing $F_{10.7}$ into radiation produced
 350 by optically thick bremsstrahlung radiation, optically thin bremsstrahlung radiation, and
 351 optically thick gyroresonance radiation. These components correspond to radiation from
 352 the chromosphere, transition region and corona, and the cores of active regions in the
 353 corona, respectively. It is the optically thin bremsstrahlung radiation (corrected $F_{10.7}$
 354 proxy), the data for which are shown in Figure 2(h), which is suggested for use in place
 355 of $F_{10.7}$ to approximate solar EUV output. A fit between the traditional $F_{10.7}$ and the
 356 corrected $F_{10.7}$ shows a linear relationship up to about $F_{10.7}$ equal to 96 solar flux units
 357 (sfu) and a power law for solar flux values above 96 sfu. The top panel of Figure 3 shows
 358 this relationship, reproduced from the fit derived in Schonfeld et al. (2019). The spread
 359 in the data around the piecewise fit is due to the conversion between the observed $F_{10.7}$
 360 and the 1 AU-adjusted $F_{10.7}$ on which these fits are defined. Converting $F_{10.7}$ to its 1
 361 AU-equivalent, applying the correction, and then reversing the 1 AU-conversion yields
 362 the tight spread, with the sharp upper and lower limits resulting from the maximum and
 363 minimum Earth-Sun separations, respectively. This index is available for the entire du-
 364 ration of $F_{10.7}$.

365 **2.3.8 $P_{10.7}$ Index**

366 Also derived from $F_{10.7}$ is the $P_{10.7}$ index, calculated by taking the mean of the real-
 367 time $F_{10.7}$ with the 81-day averaged $F_{10.7}$ index (F_{81}). This index is used in other iono-
 368 spheric models to capture solar variability, as described above, but presents a philosoph-
 369 ical dilemma by using future values of solar flux to predict TEC (Lean et al., 2016). Equa-
 370 tion (1) shows the method used to calculate the values corresponding to this input pa-
 371 rameter. Figure 2(i) shows the time series corresponding to this index.

$$P_{10.7} = (F_{10.7} + F_{81})/2 \quad (1)$$

372 **2.3.9 Solar Irradiance Platform (SIP) $E_{10.7}$**

373 The Solar Irradiance Platform (SIP, formerly the SOLAR2000 model), provides a
 374 comprehensive solar spectrum developed by the Space Environment Technologies (SET)
 375 company (<http://www.spacewx.com/solar2000.html>). The company has developed
 376 several proxies for solar activity and provides them to the research community. The $E_{10.7}$
 377 index, shown in Figure 2(j), most closely resembles the solar EUV spectrum by report-
 378 ing the flux from 1 - 105 nanometers scaled to solar flux units (sfu). The index reflects
 379 general solar activity on 27-day and solar cycle (11 year) time scales (W. K. Tobiska, 2002).
 380 The index was developed with the intention of capturing the solar cycle variability and
 381 output most directly influential on the ionosphere-thermosphere system. However, as shown
 382 in Figure 2(f), the index shows a sharp peak in late 2001 and early 2002 not reflected
 383 in the other EUV datasets. This is found to have a detrimental effect on the model as
 384 discussed below.

385 **2.3.10 Flare Irradiance Spectral Model EUV**

386 The Flare Irradiance Spectral Model (FISM) is an empirical model which estimates
 387 the solar irradiance in the EUV range with a time cadence of one day and a spectral res-
 388 olution of 0.1 nm, ten times better resolved than TIMED SEE EUV. FISM was devel-
 389 oped to improve the accuracy of space weather model estimations (Chamberlin et al.,
 390 2007). In addition, the development of this model increases temporal resolution for the
 391 sake of capturing variations due to solar flares (Chamberlin et al., 2008). Here we use
 392 version 2 of the FISM data. The proxy is available in bands from 0 to 190 nanometers,

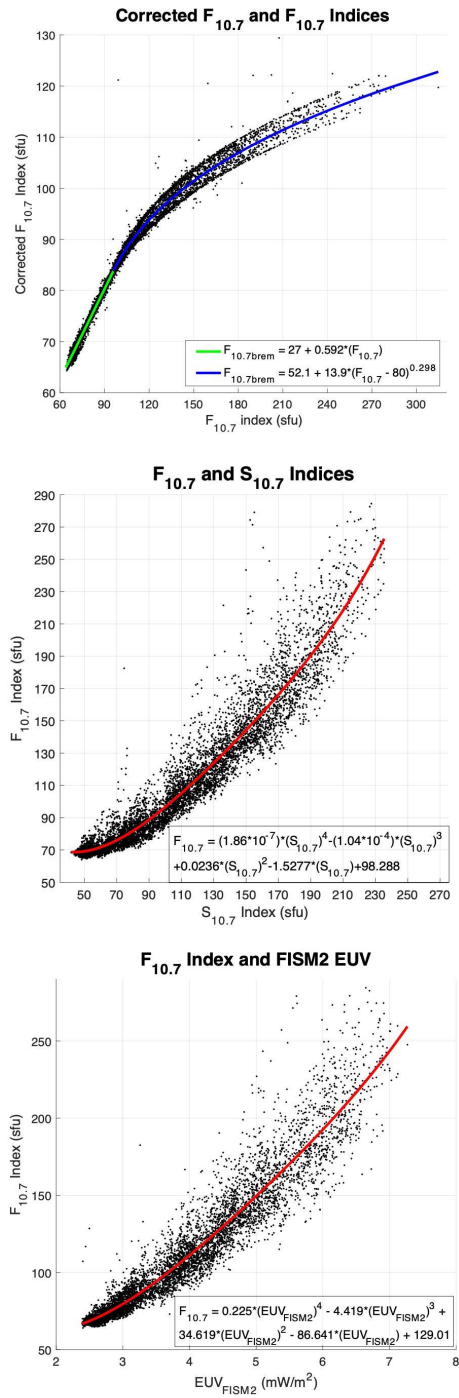


Figure 3. Verification of the fit between the corrected $F_{10.7}$ proxy and the original $F_{10.7}$, as provided in Schonfeld et al. (2019) (top). Relationship between $F_{10.7}$ and $S_{10.7}$ for the years 2000 through 2019 (middle). Relationship between $F_{10.7}$ and FISM2 EUV for the years 2000 through 2019 (bottom).

393 although, as with the TIMED SEE data, only the 0.05 to 105.05 nanometer wavelength
 394 bins are used here. The data were processed by integrating across this bandpass. Upon
 395 investigation it was found that the inclusion of higher wavelengths in the EUV range does
 396 not significantly contribute to the performance of the ionospheric model. The data are
 397 available from the LASP Interactive Solar Irradiance Data Center ([http://lasp.colorado](http://lasp.colorado.edu/lisird/)
 398 [.edu/lisird/](http://lasp.colorado.edu/lisird/)), and are shown for the 2000 - 2019 period in Figure 2(k). The relation-
 399 ship between the $F_{10.7}$ and FISM2 indices is shown in the bottom panel of Figure 3.

400 3 Formulation of the New Empirical Model

401 We construct a model of TEC variation at a given location (45°N, 0°E in this spe-
 402 cific case) as a function of solar flux, season, and geomagnetic activity through a mul-
 403 tiple linear regression fit of the observed TEC to time series of solar flux proxies (with
 404 multiple delays), seasonal oscillations, geomagnetic activity indices (with multiple de-
 405 lays), and cross-modulation of these terms. Explicitly, the model is formulated as fol-
 406 lows:

$$TEC(t, DOY) = TEC_0 + TEC_{sol}(t) + TEC_{seas}(DOY) + TEC_{geo}(t) + TEC_{cr-terms}(t, DOY), \quad (2)$$

where

$$TEC_{sol}(t) = \sum_{n=0}^{n_{sol}} a_n F(t-n) + bF^2(t); n = 0, 1, 8, 24, 36 \text{ days} \quad (3)$$

$$TEC_{seas}(DOY) = \sum_{m=1}^{m_{seas}} c_m \sin\left(\frac{2\pi DOY m}{365}\right) + d_m \cos\left(\frac{2\pi DOY m}{365}\right); m = 1, 2, 3, 4 \quad (4)$$

$$TEC_{geo}(t) = \sum_{l=0}^{l_{geo}} e_l Ap_3(t-l) + \sum_{l_1=0}^{l_{1,geo}} e_{l_1} Ap_3(t-l_1); l = 0, 3, 24, 48, 72 \text{ hours}; l_1 = 0, 48 \text{ hours} \quad (5)$$

$$\begin{aligned} TEC_{cr-terms}(t, DOY) = & \\ & \sum_{k_1=1}^3 f_{k_1} F(t) \sin\left(\frac{2\pi DOY k_1}{365}\right) + g_{k_1} F(t) \cos\left(\frac{2\pi DOY k_1}{365}\right) \\ & + \sum_{k_2=1}^4 f_{k_2} F(t)^2 \sin\left(\frac{2\pi DOY k_2}{365}\right) + g_{k_2} F(t)^2 \cos\left(\frac{2\pi DOY k_2}{365}\right) \end{aligned} \quad (6)$$

407 Equation (3) describes the TEC response to solar activity, where F is a solar ac-
 408 tivity proxy (i.e. one of the proxies described in section 2.3) and n is a temporal lag of
 409 this proxy (in days). As formulation of the model allows easy manipulation with addi-
 410 tion or exclusion of different terms, extensive testing of different lags in the solar activ-
 411 ity proxy was performed. Delay terms of 1 day, 2 days, 3 days, 4 days, 6 days, 8 days,
 412 24 days, and 36 days were considered for the solar flux terms in addition to the real-time
 413 (0 hour delay) term. Although delay terms with 2-6 days showed some statistical signifi-
 414 cance, their inclusion resulted in lower coefficients for real-time solar flux terms, but
 415 did not lead to meaningful improvement of the model. Ultimately, only the real-time,
 416 1-day delay, 8-day delay, 24-day delay, and 36-day delay terms showed highest signifi-
 417 cance, and the n listed after the formula indicates solar proxy delays that were included

418 in the current version of the model ($n = 0, 1, 8, 24, 36$ days). Note that a square term
 419 for the real-time solar proxy is also included. Equation (4) describes seasonal variation
 420 as a combination of sine and cosine functions that correspond to annual, semi-annual,
 421 4-month, and 3-month variations. Shorter-term variations (4-months, 3-months) were
 422 found to be significant and improve the description of the timing for equinoctial enhance-
 423 ments in TEC. Equation (5) describes the dependence on geomagnetic activity as a func-
 424 tion of Ap_3 index and different temporal lags of Ap_3 index. Several temporal Ap_3 lags
 425 were included in the model after extensive testing for their statistical significance, specifi-
 426 cally, 3-hr, 24-hr, 48-hr, and 72-hr. Finally, equation (6) describes the statistically sig-
 427 nificant cross-terms (e.g. amplitude modulation of solar flux and seasonal terms). This
 428 approach produces 35 fitting coefficients $a, b, c, d, e,$ and f . We note that solar flux terms
 429 and geomagnetic activity terms were standardized based on the median and standard
 430 deviation of the observed values in the 20-year period considered in this study.

431 The standardization technique is shown in equations (7) - (10), where F_{med} and
 432 Ap_3_{med} are the medians of the FISM2 EUV and Ap_3 index, respectively, calculated for
 433 each LT, and F_{std} and Ap_3_{std} are the standard deviations of the FISM2 and Ap_3 indices,
 434 respectively, calculated for each LT. Squared variables are not standardized independently,
 435 but rather are calculated by squaring the standardized linear terms. This is done to re-
 436 duce multicollinearity without affecting the correlation coefficients with other variables
 437 (Kim & Dong-Ku, 2011). We slightly modify this method by using the median rather
 438 than the mean to account for the large number of statistical outliers which exist in both
 439 the solar flux and geomagnetic datasets.

$$EUV_{FISM2}(t - n)_{stand} = [EUV_{FISM2}(t - n) - F_{med}]/(F_{std}); n = 0, 1, 8, 24, 36 \text{ days} \quad (7)$$

$$EUV_{FISM2}^2_{stand} = (EUV_{FISM2_{stand}})^2 \quad (8)$$

$$Ap_3(t - l)_{stand} = [Ap_3(t - l) - Ap_3_{med}]/(Ap_3_{std}); l = 0, 3, 24, 48, 72 \text{ hours} \quad (9)$$

$$Ap_3^2(t - l_1)_{stand} = [Ap_3(t - l_1)_{stand}]^2; l_1 = 0, 48 \text{ hours} \quad (10)$$

440 A distinctive feature of this model is its description of diurnal behavior. While most
 441 other models describe diurnal behavior as a superposition of sines and cosines with 24-
 442 hr, 12-hr, and 8-hr periods, this model is composed of 48 separate models, i.e. every 30-
 443 min bin of TEC is fitted with equations (2) - (6), resulting in 1680 fitting coefficients for
 444 a local model. This approach is similar to that used by Themens et al. (2017) and al-
 445 lows accurate description of diurnal behavior, especially the rapid TEC increase after
 446 the sunrise and decrease after the sunset. This formulation is also useful in assessing the
 447 importance of each predictor at different local times. To construct the model, we have
 448 used 90% of the available TEC data, randomly selected out of all 20 years of observa-
 449 tions. The remaining 10% of data were used for testing purposes. Statistical significance
 450 of each input parameter in equations (2) - (6) was examined based on ANOVA tables
 451 and P values. While not all UT time bins had high statistical significance for all predic-
 452 tors, all showed significance at some point during the day, and therefore were included
 453 in the model. For example, the squared 48-hour delayed Ap_3 index (Equation 5) was rel-
 454 atively insignificant from 0-4UT and 8-17UT, but highly significant (P value less than
 455 0.01) from 5-7UT and 19-24UT. Section 5.1 discusses this aspect in more detail.

456 Data inspection showed that in addition to data quality issues on the scale of a few
 457 days, long-term errors (e.g. artificially elevated readings for TEC lasting more than a

	RMSE (TECu)	MSE (TECu ²)	MAE (TECu)	MAPE (%)	Correlation Coefficient	Mean of Data-Model Difference (TECu)
SOHO EUV	3.4108	11.6338	2.0645	17.4295	0.8597	-0.1333
F10.7	2.2039	4.8570	1.4413	13.0032	0.9402	-0.0139
Mg II CWR	2.0706	4.2874	1.4044	12.8850	0.9475	-0.0379
Lyman-Alpha	2.2157	4.9094	1.4568	13.0893	0.9402	-0.0597
S10.7	2.064	4.2600	1.3516	12.2320	0.9489	-0.0135
Solar S10.7	2.1577	4.6557	1.4274	12.9051	0.9419	-0.0538
Corrected F10.7	2.5432	6.4679	1.6436	14.8091	0.9106	-0.0704
P10.7	2.1587	4.6598	1.4198	12.8312	0.9420	<i>0.0092</i>
E10.7	2.3204	5.3841	1.5038	13.7618	0.9334	-0.1104
FISM2 EUV	<i>1.9539</i>	<i>3.8177</i>	<i>1.3120</i>	<i>11.9038</i>	<i>0.9537</i>	-0.0269

Table 1. Error evaluation of the solar flux proxies for 2000 - 2019 at 45°E, 0°N. The error value corresponding to the best performing proxy in each column is in bold and italic. For all metrics besides the mean of the difference between data and model, the model which uses FISM2 EUV performs the best.

458 few days) were present in the original dataset. To account for these outlier cases, the model
 459 is built in two iterations. This involves constructing the model at each location twice in
 460 succession. After the first iteration, points satisfying the following criteria are removed
 461 from the set:

- 462 1. Data-model percentage difference exceeds 2 standard deviations.
- 463 2. Solar flux (using FISM2 EUV) and relevant delays remain below $6.5 \text{ mW}/\text{m}^2$
- 464 3. Geomagnetic index (A_p3) and relevant delays remain below 80.

465 4 Investigation of Solar Flux Proxies

466 A significant task of the current study is to determine the most suitable solar flux
 467 proxy out of those described in section 2.3 to use as input to the model. The data them-
 468 selves show noticeable differences, as displayed in Figure 2. In particular, the relative
 469 strengths of solar cycles 23 and 24 vary largely depending on proxy. For $F_{10.7}$, $S_{10.7}$, $P_{10.7}$,
 470 FISM2 EUV, TIMED SEE EUV, Lyman-alpha, and the Mg II core-to-wing ratio, the
 471 peak of solar cycle 23 (occurring, according to monthly sunspot number, in November
 472 2001) is slightly stronger than that of solar cycle 24 (April 2015). The best-performing
 473 models typically use these data as their solar flux parameters. In the corrected $F_{10.7}$, the
 474 two solar cycles show similar maximum activity. Finally, SOHO EUV, the raw $S_{10.7}$ in-
 475 dex, and especially the $E_{10.7}$ index predict significantly higher activity during the peak
 476 of solar cycle 23. Only the TIMED SEE EUV data are not available for the entire 2000
 477 to 2019 epoch, having begun operations in January 2002.

478 For each proxy, the same terms were included as parameters in the model: real-
 479 time, 24-hour delay, 192-hour (8 day) delay, 576-hour (24 day) delay, and 864-hour (36
 480 day) delay terms. The real-time solar flux parameter included both linear and quadratic
 481 terms; the delay terms were only linear. The model was developed twice for each solar
 482 flux proxy: once from 2002-2019, once from 2000-2019. This was done in order to pro-
 483 vide a meaningful comparison of the TIMED SEE EUV data to the other chosen solar
 484 flux indices. Several error metrics were used to evaluate the performance of these devel-
 485 oped models, including the root mean squared error (RMSE), mean squared error (MSE),

	RMSE (TECu)	MSE (TECu ²)	MAE (TECu)	MAPE	Correlation Coefficient	Mean of Data-Model Difference (TECu)
TIMED EUV	1.7473	3.0532	1.2279	12.5472	0.9397	-0.0030
SOHO EUV	2.7853	7.7576	1.7292	16.4171	0.8602	-0.1153
F10.7	1.8460	3.4075	1.2683	12.8598	0.9411	0.0091
Mg II CWR	1.8402	3.3863	1.2592	12.7875	0.9422	-0.0673
Lyman-Alpha	1.9153	3.6684	1.2894	12.9100	0.9363	-0.074
S10.7	1.7272	2.9831	1.1884	12.0422	0.9486	-0.0242
Solar S10.7	1.8502	3.4232	1.2631	12.7769	0.9357	-0.0359
Corrected F10.7	1.9795	3.9183	1.3743	14.1752	0.9107	-0.0452
P10.7	1.8074	3.2667	1.2504	12.6814	0.9431	-0.0016
E10.7	1.9944	3.9775	1.3361	13.5732	0.9267	-0.0972
FISM2 EUV	1.7277	2.9848	1.1717	11.8086	0.9483	-0.0288

Table 2. Error evaluation of the solar flux proxies for 2002 - 2019 at 45°N, 0°E. The error value corresponding to the best performing proxy within each column is in bold and italic. For RMSE, MSE, and the correlation coefficient, the model which uses $S_{10.7}$ performs the best. For MAE and MAPE, FISM2 EUV produces the best-performing model. For the mean of the difference between data and model, the $P_{10.7}$ index produces the best-performing model.

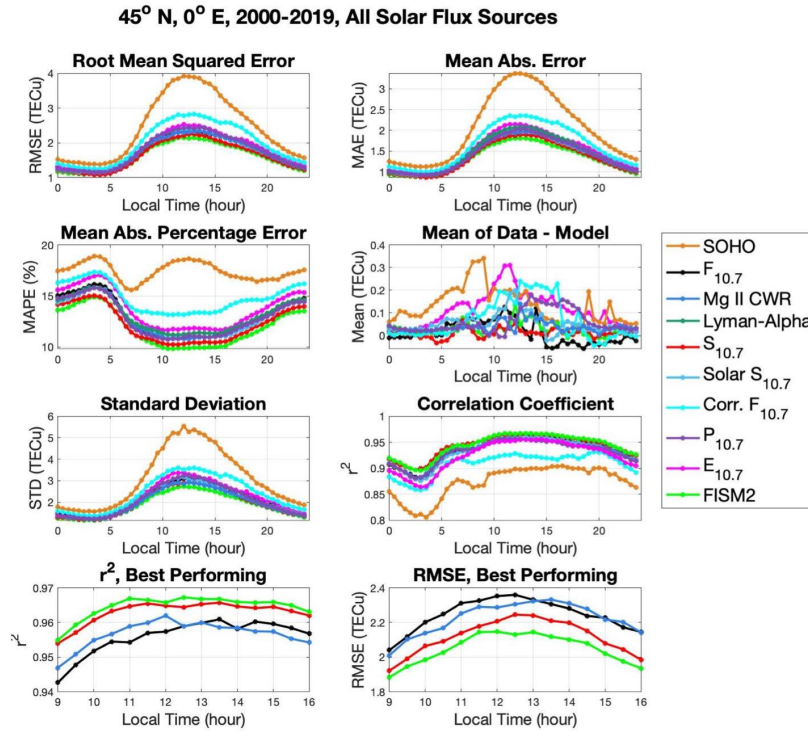


Figure 4. A comparison of the performance of solar flux proxies with a dependence on local time for 2000 - 2019.

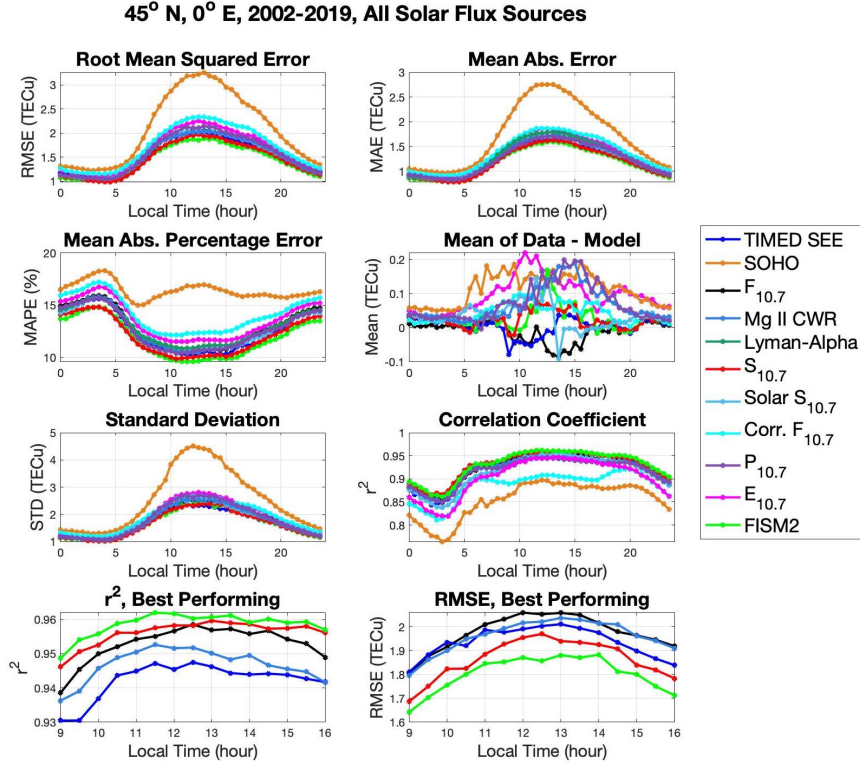


Figure 5. A comparison of the performance of solar flux proxies with a dependence on local time for 2002-2019.

486 mean absolute error (MAE), mean absolute percentage error (MAPE), correlation co-
 487 efficient (r^2), and the mean of the data-model difference. The results of error analysis
 488 for 45°N 0°E are shown in Table 1 for the entirety of the TEC dataset (2000 - 2019) and
 489 in Table 2 for the years covered by the TIMED SEE EUV data (January 2002 - 2019).
 490 We note that the errors in 2002-2019 epoch are clearly lower than in 2000-2019. This
 491 is most likely related to higher solar activity in 2000-2001 and, consequently, higher ab-
 492 solute TEC values during those years. In addition, model errors are evaluated with a de-
 493 pendence on LT, as shown in Figure 4 for the 2000 - 2019 epoch and Figure 5 for the 2002
 494 - 2019 epoch. Diurnal variation in the accuracy of the model is clearly evident for all sol-
 495 ar flux proxies, with the largest absolute errors typically observed around 12 - 13 LT
 496 and smallest errors around 5 LT, reflecting maximum and minimum values of total elec-
 497 tron content.

498 Clear differences are observed in the relative performance of each solar flux proxy.
 499 For the model which includes data from 2000 to 2019, the best-performing are the FISM2
 500 EUV, the $S_{10.7}$ index, the solar $S_{10.7}$ index, and the Mg II core-to-wing ratio. As $F_{10.7}$
 501 has been traditionally the most-used solar flux proxy, we include this proxy for compar-
 502 ison in lieu of solar $S_{10.7}$ in the bottom panels of Figure 4. $P_{10.7}$ is excluded from these
 503 panels, as well, on account of its modest performance in conjunction with the philosphical
 504 dilemma in its use described above. In comparing the model to the data on which
 505 it is built, the best-performing four proxies have root mean squared error below 2.2 TECu,
 506 mean squared error below 4.66 TECu, mean absolute error below 1.43 TECu, and cor-

507 relation coefficient above 0.94. These results are consistent with conclusions of Maruyama
 508 (2010), who investigated five types of solar flux proxies and concluded that the $S_{10.7}$ in-
 509 dex outperforms $M_{10.7}$ and $F_{10.7}$ for TEC modeling over Japan. The Mg II core-to-wing
 510 ratio also performs better than $F_{10.7}$ in application to our ionospheric model. This also
 511 agrees with the claim made by Viereck et al. (2001) in their suggestion that the Mg II
 512 data is more suitable than $F_{10.7}$ as a proxy for the solar extreme ultraviolet flux, a sug-
 513 gestion made based on data from 1978 to 2000.

514 The model built with TIMED SEE EUV data performs well, though we will mostly
 515 consider only those proxies available for the longer time period (including all of years 2000
 516 and 2001). The TIMED data do not outperform the other indices to an extent which
 517 warrants neglecting a large part of the maximum corresponding to solar cycle 23. Even
 518 for the 2002 - 2019 period covered by the TIMED SEE data, there are frequent data gaps
 519 listed by T. N. Woods (2005). Many of these are attributed to the TIMED SEE “Safe
 520 Mode.” In terms of r^2 , for daytime hours, TIMED SEE EUV rivals the SIP $E_{10.7}$. This
 521 is expected, as the two proxies represent roughly the same wavelength range and the re-
 522 moval of the time period not covered by TIMED SEE avoids the sharp peak in $E_{10.7}$ ob-
 523 served in Figure 2(j). SIP v2.38 was derived mostly with the correspondence of indices
 524 and proxies to the TIMED SEE v11 data. In terms of RMSE, for the 2002 - 2019 pe-
 525 riod, the TIMED SEE EUV performs better than all proxies except $S_{10.7}$ and FISM2
 526 EUV. Regardless, FISM2 EUV outperforms TIMED SEE EUV and other proxies in terms
 527 of all error metrics and does not suffer from the data gaps shown by TIMED SEE EUV,
 528 making FISM2 EUV the most appropriate choice of solar flux proxy as input to the model.

529 As shown in Figure 4, the model built using SOHO SEM EUV is generally the worst-
 530 performing. This is evident across all error metrics used with the exception of the mean
 531 of the data-model difference. Although the reason for this is not clear, we note that the
 532 ratio between solar maxima 23 and 24 for SOHO SEM solar flux is higher than for other
 533 formulations of solar flux. In addition, the SOHO SEM flux during the solar minimum
 534 2018-2019 is lower than during the solar minimum of 2008-2009 (see Figure 2). While
 535 we cannot completely rule out some uncorrected degradation of the SEM data during
 536 the last several years, comparison of SOHO SEM with SDO EVE measurements shows
 537 good agreement of observations at least until the end of 2013 (Wieman et al., 2014).

538 To indicate an overall relationship between TEC and different solar data, Figure
 539 6 presents a relative deviation in the ratio TEC_{mod}/F_{sol} for four of the best-performing
 540 formulations of solar flux at 6 LT (top) and 15 LT (bottom). The relative deviation is
 541 determined as

$$\Delta \frac{TEC_{mod}}{F_{sol}} = \frac{\frac{TEC_{mod}}{F_{sol}} - (\frac{TEC_{mod}}{F_{sol}})_{mean}}{(\frac{TEC_{mod}}{F_{sol}})_{mean}} \quad (11)$$

542 where TEC_{mod} is the TEC value provided by the model and F_{sol} is the solar flux
 543 proxy used in that model. We note that the same behavior in relative deviation is seen
 544 in TEC observations, though it is more clear in the modeled TEC . For 6 LT, relative
 545 deviation is simple and shows a strong annual variation, with wintertime minimum and
 546 summertime maximum, and a weak solar activity dependency. For 15 LT, the relative
 547 deviation is more complex and is dominated by two main features: solar activity vari-
 548 ation and seasonal variation. Positive values are seen for high solar activity levels and
 549 negative values for lower solar activity levels, probably reflecting the non-linear nature
 550 of TEC response to increases in solar flux. The seasonal response is more complex and
 551 shows a minimum in TEC_{mod}/F_{sol} in winter and two peaks during the equinoxes. This
 552 behavior reflects an annual variation in TEC with lower TEC in winter than in sum-
 553 mer, and a semiannual variation in TEC which is partially related to semiannual vari-
 554 ation in neutral composition and density. All four formulations of solar flux show these
 555 features, though dependence on solar activity level is strongest for the $MgII$ index and

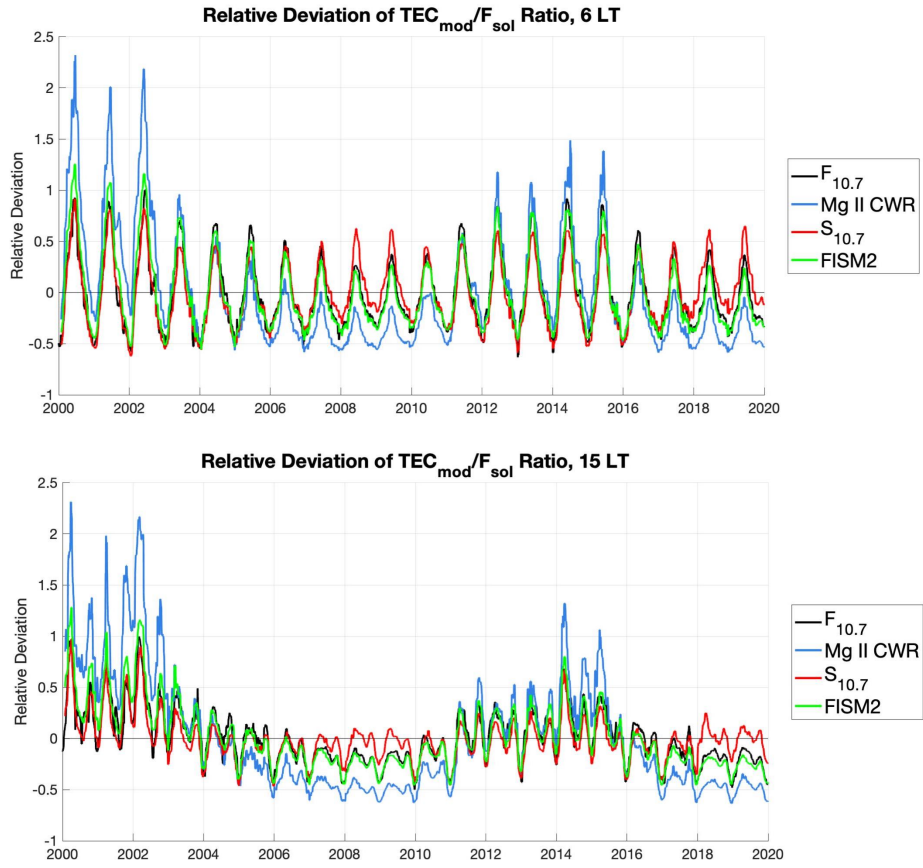


Figure 6. Relative deviation of TEC_{mod}/F_{sol} ratio for different solar flux proxies at 6 LT (top) and 15 LT (bottom).

556 weakest for the $S_{10.7}$ index. In developing the $S_{10.7}$ index, SET artificially removes about
 557 30% of the energy at the top of the atmosphere during solar minimum by reducing the
 558 solar value of $S_{10.7}$ in order to correct for thermospheric cooling and to best match the
 559 orbital drag above 200 km for the NORAD catalog, where $S_{10.7}$ is primarily used in op-
 560 erations. Apparently, this adjustment affects the TEC values as well, as the $S_{10.7}$ index
 561 is found to perform very well for TEC modeling and only slightly worse than FISM2 EUV.

562 To summarize, our analysis of the several formulations of the model differing only
 563 in the solar flux proxy suggest that FISM2 EUV is statistically the best choice to use
 564 in the final formulation of the model. Models built with this proxy outperform those de-
 565 veloped with datasets traditionally used to reflect solar activity, $F_{10.7}$ in particular. Not
 566 only does FISM2 EUV show that it is the most appropriate proxy to use through sta-
 567 tistical analysis, but also according to physical application to the system being modeled.
 568 These data are developed to directly reflect the solar output between 0.05 to 105.05 nanome-
 569 ters. This includes the 26 to 34 nanometer range, the subset of the extreme ultraviolet
 570 range absorbed by atomic oxygen above 200 kilometers (W. K. Tobiska et al., 2008), [IS
 571 14222] which corresponds mostly to the F-region ionosphere. From a physical point of
 572 view, it is reasonable that an index reflecting the solar irradiance in the bandwidth re-
 573 sponsible for a large portion of ionization in the ionosphere (in addition to other wave-
 574 lengths in the EUV range) should produce the best-performing model. $S_{10.7}$ reflects the
 575 26 to 34 nanometer range, but does not cover other potentially relevant wavelengths in
 576 the EUV range. FISM2 EUV, therefore, is ultimately the dataset used to characterize
 577 solar flux in the final formulation of the model. For historical purposes and for compar-
 578 ison with other models, we also retained the version of the model using $F_{10.7}$, as $F_{10.7}$
 579 proxy has been traditionally used for thermospheric and ionospheric modeling.

580 5 Evaluation of Model Performance

581 5.1 Performance Metrics

582 It was concluded in Section 4 that the model with FISM2 EUV as a solar flux in-
 583 dex performs better than with other solar flux surrogates. In this section we examine
 584 in more detail performance of the model with the FISM2 EUV data. A variety of met-
 585 rics are used to examine different features in the models' performance, with several of
 586 them already presented in Figures 4 and 5. The top panel of figure 7 shows a scatter plot
 587 of the observed and modeled TEC for all conditions, together with a linear fit and sev-
 588 eral performance metrics. The RMSE of the model is 1.9539 TECu. We note that this
 589 is lower than $RMSE = 2.5-3.0$ TECu obtained by Feng et al. (2019) at mid-latitudes,
 590 even though Feng et al. (2019) used highly smoothed IGS TEC maps with inherently
 591 lower variability in TEC data. In a study which is closer to our effort, when the empir-
 592 ical TEC model was constructed based on high-resolution observations over middle lat-
 593 itudes in Japan, the RMSE is equal to 3.3-3.4 TECu (Maruyama, 2010). The higher ac-
 594 curacy of our model is thought to result from a more detailed description of solar flux,
 595 seasonal and local time behavior, and inclusion of geomagnetic activity effects.

596 The bottom panel of Figure 7 shows a scatter plot of the observed and modeled
 597 TEC for all conditions for the model developed using $S_{10.7}$ as the solar flux input pa-
 598 rameters. This is the second-best-performing model of those developed using the formu-
 599 lation for model construction defined here. The error metrics corresponding to this model
 600 are less favorable than those for the model developed using FISM2 EUV, though both
 601 models perform better than previous models referenced above which provide error met-
 602 rics for this latitude (Feng et al., 2019; Maruyama, 2010).

603 Figure 8 illustrates the performance of the TEC model with season and local time
 604 using common error metrics such as mean absolute percentage error (MAPE, top), root
 605 mean square error (RMSE, middle), and root mean square percentage error (RMSPE,

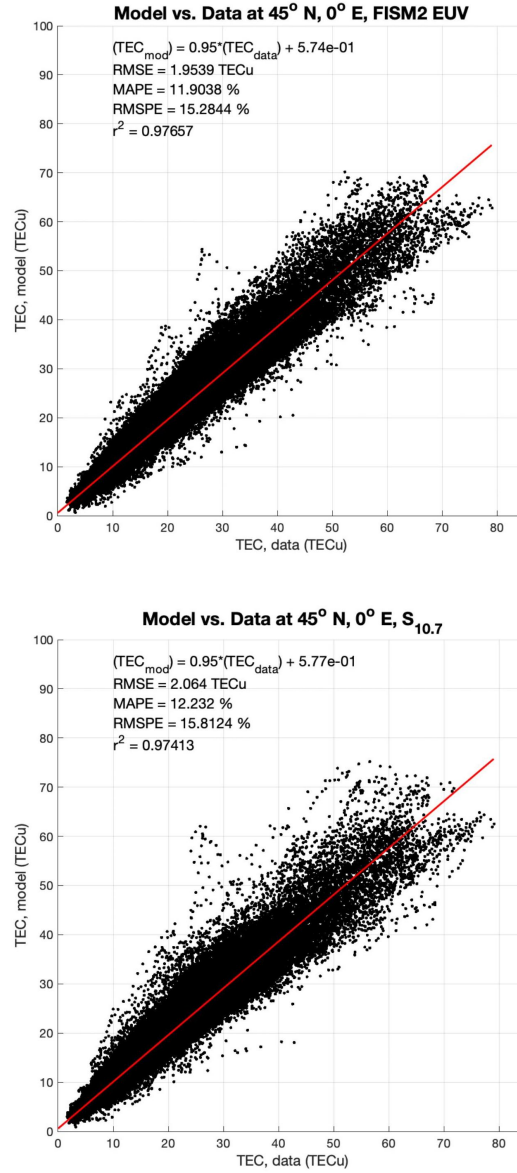


Figure 7. Scatter plot showing the relationship between observed and modeled TEC for the model built with FISM2 EUV as the solar flux proxy (top). Scatter plot showing the relationship between observed and modeled TEC for the model built with $S_{10.7}$ as the solar flux proxy (bottom).

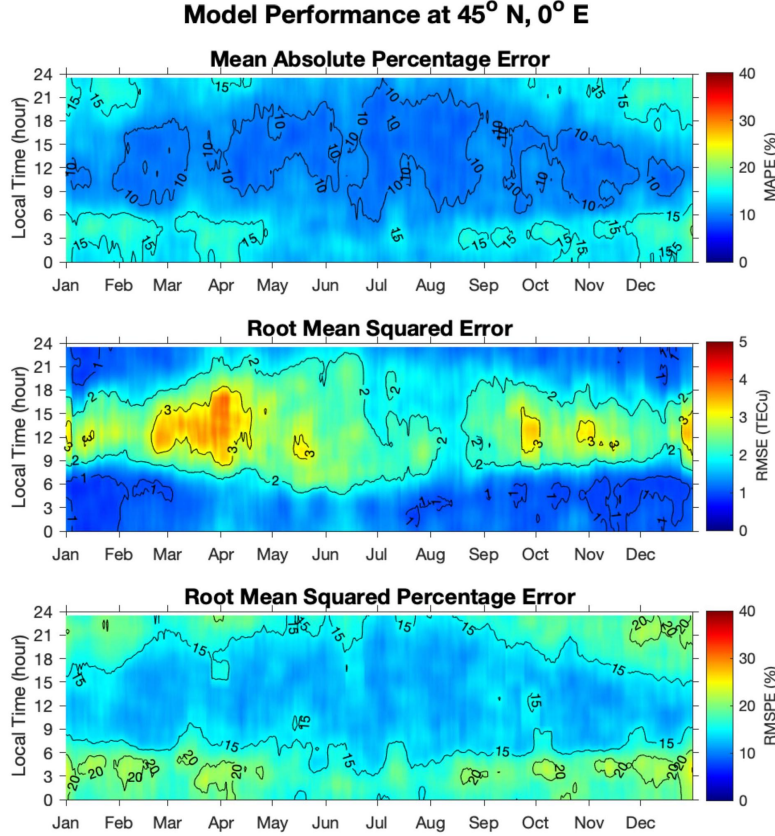


Figure 8. Performance of the TEC model in terms of mean average percentage error (MAPE, top), root mean square error (RMSE, middle) and root mean square percentage error (RMSPE, bottom) as a function of season and local time.

606 bottom). In figure 8, all metrics are calculated independently for each 30-min local time
 607 bin with a sliding 10-day window. The daytime MAPE is mostly within 8-13% for all
 608 seasons, indicating that the model does not have seasonal biases and properly reflects
 609 seasonal variation in TEC. The nighttime MAPE increases to 15-17% due to the decrease
 610 in TEC at night, but does not reach 20%. The RMSE variation (middle panel) shows
 611 the opposite local time behavior, again following diurnal variation in TEC, and varies
 612 mostly within 2-3 TECu for daytime and 0.5-1.5 TECu at night. The increase in RMSE
 613 in March-April and September- October is related to a combination of the semi-annual
 614 variation in TEC, i.e. equinoctial enhancement, and elevated levels of geomagnetic ac-
 615 tivity. The RMSPE closely follows the variation in MAPE and varies within 12-15% dur-
 616 ing daytime and 15-20% at night. Overall, the model does not show seasonal or local time
 617 biases, and seasonal or local time variations in considered metrics are consistent with such
 618 variations in TEC.

619 Figure 9 presents more details on fitting coefficients (left panels) and P values (right
 620 panels) for several terms reflecting geomagnetic activity (top) and solar flux (bottom).
 621 For geomagnetic activity, the largest coefficients are real-time Ap_3 and Ap_3 with a 3-hour
 622 delay; they reach maximum values during daytime hours (9-18 LT). Note that the co-
 623 efficient for real-time quadratic Ap_3 is negative, thus decreasing the influence of real-time
 624 Ap_3 . Overall, the combination of terms indicates positive coefficients for real-time Ap_3

625 and Ap_3 with 3-hour delay for daytime hours and mixed or negative results around dawn
 626 (3-7 LT), with a non-linear impact of Ap_3 variations on TEC. This dependency corre-
 627 sponds to a positive storm effect (increase in electron density and, subsequently, in TEC)
 628 occurring at mid-latitude locations during daytime shortly after an increase in geomag-
 629 netic activity, and mixed or negative storm effect (decrease in TEC) after an increase
 630 in geomagnetic activity occurring at dawn. The positive ionospheric storms at middle
 631 latitudes are typically observed in the initial phase of the storm and are most likely to
 632 occur at longitudes that are in the ionization production dominated morning-noon lo-
 633 cal time sectors during the onset of geomagnetic storm (Próls, 1995; Lu et al., 2008; Balan
 634 et al., 2010). Positive storm effects are driven by combined effects of equatorward wind
 635 and prompt penetration electric fields that lift the ionospheric plasma to higher altitudes
 636 with lower recombination rates. Our results are fully consistent with earlier studies of
 637 positive storm effects. Study of storm effects by Thomas et al. (2016) noted first emer-
 638 gence of weak negative storm effects 3-6 hours after the storm onset in the dusk and dawn
 639 regions. Our results of weak negative Ap_3 coefficients around dawn are also consistent
 640 with Thomas et al. (2016) study. We also note a pronounced 3-hr variation in coefficients
 641 for Ap_3 and Ap_3 with 3-hr delay; this variation has the opposite behavior (increase in
 642 the Ap_3 coefficient at a time of decrease of the coefficient for Ap_3 with 3-hour delay). This
 643 most likely reflects the competing nature of temporal delays in TEC to a geomagnetic
 644 storm and points to the shortcomings of the Ap_3 index; an index with higher temporal
 645 resolution than the 3-hr resolution of Ap_3 is required to better resolve TEC changes due
 646 to geomagnetic activity, as in the example of using Dst for 1-hour time resolution in the
 647 JB2008 model during storm periods. The coefficient for Ap_3 with 24-hour delay (black
 648 line in top left panel of Figure 9) is negative and highly significant (P values well below
 649 0.05) for all local times. This corresponds to a well-known negative storm effect in the
 650 mid-latitude ionosphere occurring the day after a geomagnetic storm (Mendillo, 2006;
 651 Wood et al., 2016). The coefficient for Ap_3 with 48-hour delay is also negative and sta-
 652 tistically significant for all local times. Moreover, we found that the coefficient for Ap_3
 653 with 72-hour delay is statistically significant, especially for nighttime hours, although
 654 lower than the coefficient for Ap_3 with 24-hour delay. Physically, this corresponds to long-
 655 lasting negative storm effects that are weaker but still can be identified 48 hours and even
 656 72 hours after the storm. Our empirical model is expected to capture these negative storm
 657 effects.

658 The dependence of TEC on solar flux (lower panels of Figure 9) is more straight-
 659 forward. Coefficients and P values for FISM2 EUV and $S_{10.7}$, the solar flux indices which
 660 produce the best-performing models, are shown. Coefficients for real-time solar flux and
 661 all delays are positive for most local times, but largest for daytime hours, indicating an
 662 obvious connection: the increase in TEC in response to increase in solar radiation. For
 663 FISM2 EUV, a larger response is observed during daytime in the 24-hour delay term than
 664 in the real-time solar flux term. The opposite effect is observed for the $S_{10.7}$ coefficients.
 665 The combined effects of contributions from both linear and quadratic terms for real-time
 666 solar flux are lower during daytime than for FISM2 EUV with a 24-hour delay, and the
 667 two are comparable for nighttime from 0-6 LT. From 18-24 LT, the real-time linear and
 668 quadratic coefficients combined are larger than the 24-hour delay coefficients, the lat-
 669 ter of which are negative from 21-24 LT. The real-time $S_{10.7}$ coefficients are lower than
 670 the 24-hour delay from 0-5 LT and higher from 18-24 LT; from 20-24 LT, the 24-hour
 671 delay term is negative as it was in the case of the FISM2 EUV.

672 Studies of the thermospheric response to the $S_{10.7}$ index found that thermospheric
 673 density correlates best with $S_{10.7}$ with a 24-hour delay (B. R. Bowman et al., 2008b),
 674 which is consistent with the atomic oxygen thermal conduction timescale in the thermo-
 675 sphere. Higher coefficients for the real-time $S_{10.7}$ index in our model for TEC represent
 676 the prevalence of a rapid response of ionospheric electron density to ionizing radiation.
 677 Longer time scales - in particular, solar flux with 24-hour delay and 192-hour, 576-hour,
 678 and 864-hour delays - represent the temporal scales of thermospheric response to ion-

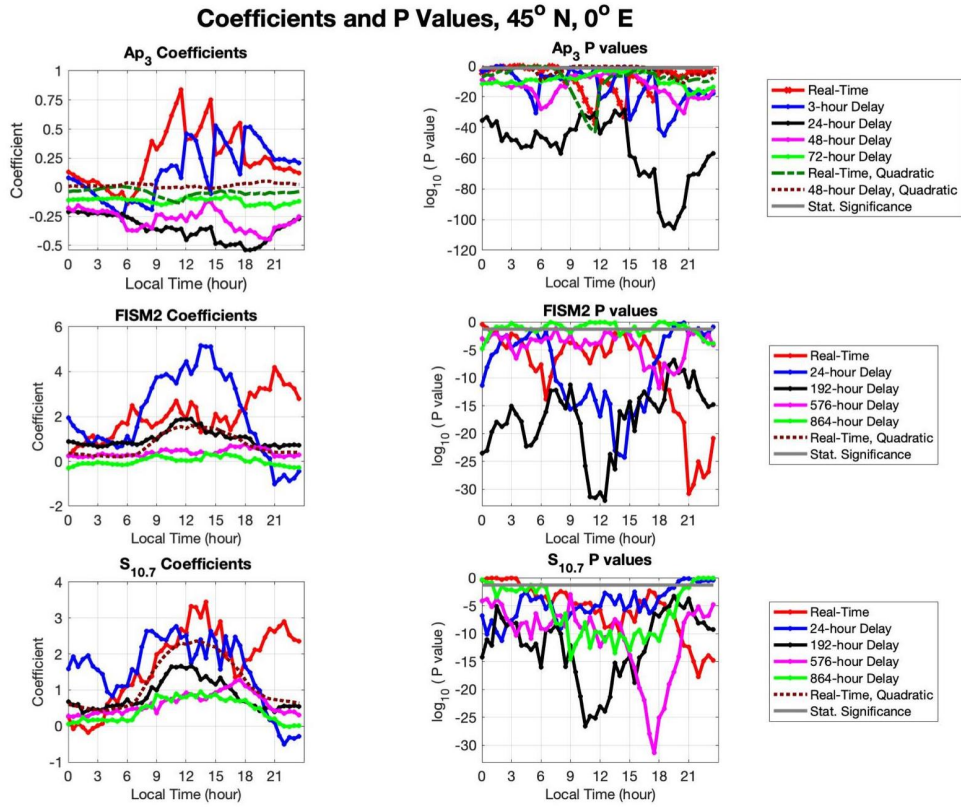


Figure 9. Modeling coefficients (left) and P values (right) for terms describing dependency on geomagnetic activity (top panels), FISM2 EUV (center panels), and $S_{10.7}$ (bottom panels). The two solar flux datasets are used to develop independent models and inserted here for comparison; the coefficients and P values corresponding to Ap_3 are mostly independent of the solar flux parameter used.

679 ionizing radiation. However, in the model with FISM2 EUV as the solar flux index, the 24-
 680 hour delay term has larger coefficients during daytime than real-time solar flux. This sug-
 681 gests a higher contribution from the delayed thermospheric response to ionizing radia-
 682 tion in this model. Maruyama (2010) has demonstrated that the delayed response of TEC
 683 to solar irradiance is different for different solar proxies; in their study, SSN and the $F_{10.7}$
 684 proxy perform better with a 2-day delay, while the $S_{10.7}$ and Mg II indices performed
 685 better with a 1-day delay. Our study suggests that not only is the 1-day delay term sig-
 686 nificant for FISM2 EUV, but it is more so than for the real-time term. Our test also in-
 687 dicates that a temporal delay of 144 hours has some statistical significance for certain
 688 local times. However, this term does not lead to a marked increase in the performance
 689 of the model, and therefore was not included in the current version of the model. De-
 690 lay terms of 48, 72, and 96 hours do not show statistical significance. Similar to Lean
 691 et al. (2016), we found that inclusion of solar flux terms with several delays decreases
 692 the need for 81-day smoothed values, as inclusion of an 81-day smoothed solar flux term
 693 does not improve the model. Several studies have indicated that the combined use of sev-
 694 eral proxies of solar activity improved the empirical model in comparison with a single
 695 proxy (Maruyama, 2010, 2011; Lean et al., 2016). We have not explored the use of the
 696 combined proxies in this study.

697 We also validate our model through comparison with TEC observations in the year
 698 2020. As our model was developed using data collected in 2000-2019, observations in the
 699 year 2020 represent an independent dataset that was not used for model development.
 700 Figure 10 presents TEC observations (top panel), predictions from our model (middle
 701 panel), and data-model differences in TECu (bottom panel) for January - March 2020.
 702 Blue lines indicate variations in the FISM2 EUV index, while black lines indicate vari-
 703 ations in Ap_3 index. We note that the Jan-Mar 2020 conditions represent very low so-
 704 lar activity and serve as an extreme case for comparison. Figure 10 shows that our model
 705 accurately captures diurnal variation in TEC, with peak TEC predicted for 12-15 LT,
 706 in agreement with observations. The model also properly describes seasonal variation,
 707 a gradual increase from low winter-time TEC to the equinoctial peak in late March. This
 708 time period also has several minor increases in geomagnetic activity, which nevertheless
 709 can produce significant ionospheric variations during low solar activity conditions. Our
 710 model properly captures the increase in daytime TEC observed on Feb 6-7 in response
 711 to a prolonged increase in geomagnetic activity ($Ap_3 = 15-27$, $Kp = 3.0-4.0$), and on Feb
 712 18, 19, and 21 ($Ap_3 = 18-27$). It also describes reasonably well the ionospheric response
 713 to a short-lived increase in Ap_3 that was observed only at one Ap_3 value (Mar 19, Ap_3
 714 $= 32$ at 1.5UT and $Ap_3 = 9$ at 4.5 UT). The largest data-model differences are observed
 715 in March and could be related to unresolved variations due to an increase in geomag-
 716 netic activity and/or due to ionospheric oscillations with multi-day periods. For exam-
 717 ple, upward propagating planetary waves with 5-6 day periods have maximum ampli-
 718 tudes during the equinox and could potentially affect electron density, especially for so-
 719 lar minimum conditions (Gu et al., 2018; Yamazaki et al., 2018; Qin et al., 2019). Our
 720 model is not expected to capture this type of influence on TEC. The RMSE for the en-
 721 tire 3-month period is 1.0022 TECu, in line with what would be expected for low solar
 722 activity. Overall, the model performs very well for these extreme solar minimum con-
 723 ditions and is expected to perform even better for more typical conditions.

724 Figure 11 presents a prediction of TEC variation with season and local time for dif-
 725 ferent levels of solar activity and different formulations of the model, with the FISM2
 726 EUV index (left panels) and $F_{10.7}$ proxy (right panels). The strongest feature in seasonal
 727 dependence is semiannual variation, with TEC peaks occurring in late March and mid-
 728 October for moderate and high levels of solar flux (bottom four panels). This semian-
 729 nual variation in TEC is closely related to semiannual variation in thermospheric com-
 730 position and density (Fuller-Rowell, 1998; Rishbeth et al., 2000; B. R. Bowman et al.,
 731 2008b; Jones et al., 2018) and has been historically reported in ionospheric data (Richards
 732 (2001) and references therein). For moderate to high levels of solar flux, TEC is higher

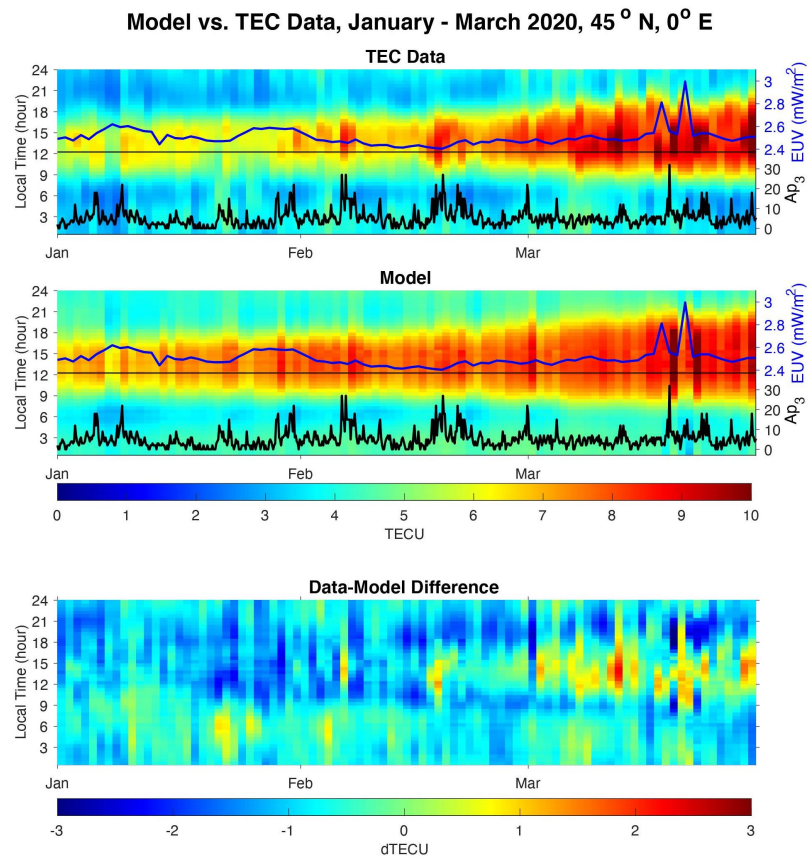


Figure 10. TEC observations (top), model predictions (middle) and data-model difference (bottom) for January-March 2020. Variations in FISM2 EUV (blue line) and Ap_3 index (black line) show that this period had extremely low solar activity with several minor geomagnetic disturbances.

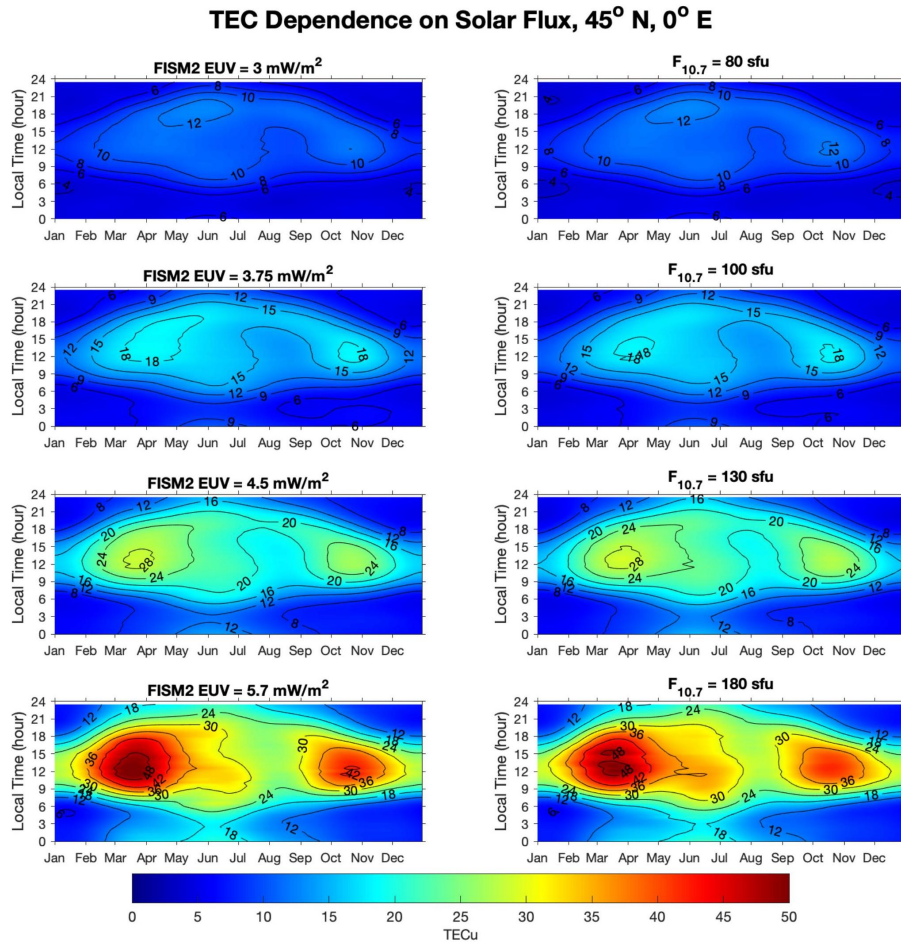


Figure 11. Model predictions of TEC variations with season and local time for different levels of solar activity. Left panels show the output for a model using FISM2 EUV, right panels show a model using $F_{10.7}$ index

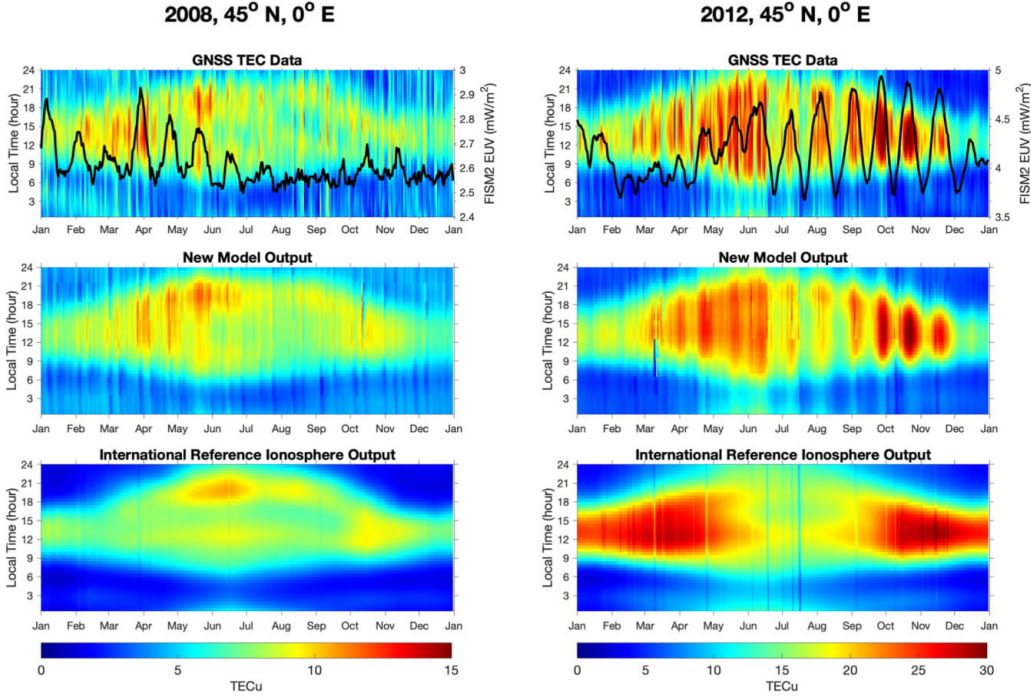


Figure 12. A comparison of GNSS TEC data (top panels), new model output (middle panels), and IRI-2016 output (bottom panels) for 2008 (left column) and 2012 (right column) at 45°N, 0°E. The FISM2 EUV for 2008 and 2012 is included for comparison to periodic fluctuations in TEC output.

733 during the spring equinox than during the fall equinox; this feature has been observed
 734 in, for example, COSMIC data (Burns et al., 2012). For moderate to high solar flux, peak
 735 values of TEC are predicted around local noon for winter and equinox conditions. How-
 736 ever, for summer conditions, morning (8-11 LT) and evening (17-19 LT) peaks are pre-
 737 dicted starting in May and June, shifting to a well pronounced evening peak in July through
 738 September. This local time behavior is particularly well pronounced for low solar flux
 739 conditions (top panels), when it dominates seasonal variation to the point where March
 740 peak in TEC does not develop. Overall, the new TEC model properly predicts numer-
 741 ous ionospheric features that are consistent with previous observations of ionospheric vari-
 742 ations with solar flux, season, and local time. This demonstrates the utility of the model
 743 for in-detail studies of such features.

744 **5.2 Comparison with International Reference Ionosphere**

745 The International Reference Ionosphere (IRI, available at irimodel.org) provides
 746 an empirical model of the ionosphere with outputs of monthly averages of the electron
 747 density, electron temperature, ion temperature, ion composition, and other parameters
 748 between 50 and 2000 kilometers altitude (Bilitza, 2004; Bilitza et al., 2014, 2017). The
 749 model is a result of the long-term effort by international research community and col-
 750 laboration between the Committee on space Research (COSPAR) and the International
 751 Union of Radio Science (URSI).

752 For comparison to our model, we use the most recent version, IRI-2016. The 2012
 753 update to the IRI model had previously provided improvements in the representations
 754 of electron density, electron temperature, and ion composition according to Bilitza et al.
 755 (2014). These improvements are attributed to updates in ionosonde design and data anal-
 756 ysis techniques, including, notably, the representation of seasonal and solar flux variabil-
 757 ity response. The IRI-2016 model also uses $F_{10.7}$, the sunspot number (R), and the ionosonde-
 758 based ionospheric global index (IG) as solar flux and ionospheric indices (Bilitza et al.,
 759 2017). Major improvements of IRI-2016 over IRI-2012 are described by Bilitza et al. (2017)
 760 and include new model options for $h_m F_2$ and an improvement of the representation of
 761 topside ion densities at the extremes of solar activity. In addition, this update includes
 762 progress in developing the IRI Real-Time model. Few differences are observed between
 763 IRI-2012 and IRI-2016 in terms of the structure of TEC output.

764 The IRI-2016 model includes $F_{10.7}$ and F_{81} (the 81-day averaged $F_{10.7}$ using 40 days
 765 prior to and following the date in question) as an optional input. Varying these param-
 766 eters does not change the output of the model significantly, however, as IRI uses the 12-
 767 month running means of an ionosphere-effective solar index (IG12), sunspot number (Rz12),
 768 and other solar flux proxies as the default values to capture variations in solar flux (Gulyaeva
 769 et al., 2018).

770 Figure 12 shows the comparison between the GNSS TEC data, our model output,
 771 and the IRI-2016 output for a year of low solar flux (2008, left panel) and high solar flux
 772 (2012, right panel). FISM2 EUV data, used as the solar flux input to our model, is plot-
 773 ted in the top panels as a black line. Several notable differences are present.

774 The most significant difference observed is the presence of short-term fluctuations
 775 in TEC in our model and the raw data, particularly during a high solar flux year such
 776 as shown in the right panel of Figure 12. This periodicity in TEC shown in the data and
 777 our model appears to match the solar rotation period of 27 days. The IRI model does
 778 not show this periodicity, presumably because of a lower direct dependence on solar flux.
 779 The difference is less present in a low solar flux year, as represented in the left panel of
 780 Figure 12.

781 We compare the local time dependence of TEC in the data, new model, and IRI-
 782 2016. The right panel of Figure 12 shows that, during a year of high solar flux (2012),
 783 the spring and autumn peaks in TEC occur around 12 LT for the data and both mod-
 784 els. During a low solar flux year (2008), an early-April peak in TEC occurs in the data
 785 and new model around 12 - 14 LT (Figure 12, left panel). IRI-2016 does not predict this
 786 peak, and in fact shows little LT variation in TEC at this point in the year, possibly be-
 787 cause it does not capture the ionospheric response to a short-term increase in solar flux
 788 as shown in the left panel of Figure 12. Both IRI-2016 and our model correctly predict
 789 a second peak in TEC that occurs around 18 - 22 LT in May through September. An-
 790 other local time peak in the late spring and summer, observed at 9 - 10 LT, is well pre-
 791 dicted by our model. However, IRI expects it to occur later, around 12 LT. The autumn
 792 peak for the data and both models is relatively consistent in LT, occurring around 12
 793 - 14 LT. Under low solar flux conditions, the IRI model generally underestimates night-
 794 time TEC values, while our model represents them well. During the spring of a high-solar
 795 flux year, the IRI model overestimates daytime TEC, while underestimating daytime TEC
 796 from June to August. Our model shows a significant improvement in prediction of TEC
 797 during these times.

798 Differences in seasonal variation are also present. For a year of low solar flux (2008),
 799 IRI predicts twice-daily enhancement in TEC in June, and a fall equinox peak in mid-
 800 October around 12 - 14 LT. Our model reflects similar seasonal peaks but captures an-
 801 other period of elevated TEC in April which corresponds to an increase in solar flux. For
 802 a year of high solar flux, as shown in the right panel of Figure 12, the spring peak in IRI
 803 is both earlier and more substantial than in either our model or the TEC data. IRI shows

804 a higher peak in TEC centered around mid-March, whereas the most elevated TEC in
 805 the new model and data occurs later, in late May and early June. The autumn peak in
 806 TEC as predicted by IRI is slightly later in the year, in early to mid November, whereas
 807 the data and model show an autumn peak in mid-October. Perhaps most notably, IRI
 808 overestimates daytime TEC during the winter months (December, January, and Febru-
 809 ary in particular) during the year of high solar flux. Our model describes TEC levels dur-
 810 ing these months well.

811 Similar limitations in the predictions made by the IRI model are described in other
 812 studies. Li et al. (2016) make a comparison similar to ours above, but for the years 2009
 813 and 2013, using IRI-2012 to TEC-GIM maps at the mid-latitude Beijing Fangshan sta-
 814 tion (BJFS) in China (39.6° N). They note that the periodicity of TEC-IRI more closely
 815 resembles TEC-GIM during the low solar flux year, while during a high solar flux year,
 816 main differences between GIM and IRI-2012 may be largely attributed to periodic (an-
 817 nual, semiannual, three-monthly, and four-monthly) components and the solar activity
 818 component. Nighttime underestimation and daytime overestimation of TEC by IRI-2012
 819 during a high solar flux year are also noted. In this study, the IRI-2012 solar activity com-
 820 ponent shows very little variation over the course of the year, and the IRI-2012 depen-
 821 dence on periodic components is strongly muted when compared to GIM-TEC. Large
 822 differences are observed, in particular, between the TEC-GIM and TEC-IRI annual and
 823 three-monthly components during 2013. This suggests that the inclusion of a major de-
 824 pendence on both periodic and solar activity components may yield better agreement
 825 with the data, particularly during years of relatively high solar flux. Similar patterns are
 826 observed in comparison of IRI-2016 to our model and the GNSS TEC data, as described
 827 above.

828 As described by Tariku (2016), who studies IRI-2012, this version tends to under-
 829 estimate TEC at mid-latitudes during years of low solar flux, and often overestimates
 830 the data during years of higher solar flux. In a comparison of IRI-2016 and IRI-2012 to
 831 TEC data over mid-latitude locations in the continental United States, Tariku (2019)
 832 notes that IRI-2016 is better able to estimate TEC during evening hours than IRI-2007
 833 and IRI-2012, but largely overestimates TEC when solar flux increases during the day.
 834 This is particularly clear during periods of low solar flux, including the December sol-
 835 stice. Differences between IRI-2012 and IRI-2016 are attributed to IRI-2012's omission
 836 and IRI-2016's subsequent addition of the plasmaspheric TEC, which contributes to over-
 837 all TEC more significantly during nighttime (Kumar, 2016). Zakharenkova et al. (2015)
 838 similarly shows that the IRI-Plas model, an extension of IRI accounting for plasmaspheric
 839 contributions prior to the development of IRI-2016, overestimates TEC at middle lat-
 840 itude even during periods of low to moderate solar flux. The limitations of IRI-2016 are
 841 attributed to the new model options in estimating $h_m f_2$ directly as well as the improved
 842 representation of topside ion densities at extremes of solar activity, as discussed in (Bilitza
 843 et al., 2017; Tariku, 2019). Of particular concern to Kumar (2016) is the difference be-
 844 tween EUV (particularly 26 - 34 nm) and the solar flux parameters used in the IRI model;
 845 in IRI-2012, the TEC output depends on $N_m f_2$ and $h_m f_2$, which depend on IG12 and
 846 Rz12 respectively. Many sources cite that differences between IRI-TEC and TEC data
 847 tend to be less significant at mid-latitudes than low and high latitudes (Kumar, 2016;
 848 Kumar et al., 2015; Alcay et al., 2017).

849 Our model addresses several of the limitations of IRI addressed by these studies
 850 and our discussion above. Most notably, the 27-day periodic variations in TEC during
 851 years of high solar flux are well captured by our model, while both IRI-2012 (Li et al.,
 852 2016) and IRI-2016 fail to describe it. Our model captures the daytime and nighttime
 853 amplitude as well as the seasonal and local time position of the TEC peak, a notable im-
 854 provement over the nighttime underestimation, daytime overestimation, and seasonal and
 855 local time limitations of IRI.

6 Summary

Development of forecasting capabilities of the near-Earth space environment remains one of the important topics in space weather research. As the accuracy of existing empirical models falls short of what is required to meet the needs of space weather services and the needs of academic research community, development of new empirical models with increased accuracy and spatio-temporal resolution is required.

This work presents the first stage in the development of a new empirical TEC model that aims to provide high temporal and spatial resolution. The model is formulated at a single location, $45^\circ N$ and $0^\circ E$, and aims to accurately describe variations in TEC with solar cycle, season, LT, and geomagnetic activity with 30-min resolution. The model is constructed using 20 years of high-resolution TEC observations from the CEDAR madrigal database (2000-2019) and uses multiple temporal delays (ranging from 24 hrs to 36 days for solar flux and from 3 hrs to 72 hrs for geomagnetic activity) to describe TEC dependence on solar EUV and geomagnetic activity.

The central focus of the current work is investigation of different descriptions of solar flux proxies with the goal to select the most appropriate proxy to describe TEC variations. This study examined 11 descriptions of solar flux surrogates and measurements (TIMED SEE EUV, SOHO EUV, $F_{10.7}$, the Mg II core-to-wing ratio, the Lyman-alpha composite, $S_{10.7}$, raw $S_{10.7}$, corrected $F_{10.7}$, $P_{10.7}$, $E_{10.7}$, and FISM2 EUV) for two time periods, 2000-2019 and 2002-2019, using the same formulation of the empirical model. Our results indicate that the FISM2 EUV index performs the best, closely followed by the $S_{10.7}$ index, the $F_{10.7}$ proxy, and the Mg II index. As inclusion of the years 2000 to 2001 is important for proper description of TEC variations during high solar activity, the absence of TIMED EUV data prior to 2002 limits its applicability.

The overall RMSE of the model is 1.9539 TECu, lower than that of comparable empirical models. The RMSE of the new empirical model varies within 0.5-1.5 TECu at night and 2-3 TECu during the daytime. MAPE (Mean Absolute Percentage Error) varies within 8-13% during daytime and within 15-17% at night, without seasonal biases. Higher accuracy is attributed to the combined influences of more accurate descriptions of TEC dependency on solar flux, season, local time, and geomagnetic activity.

The model represents well features such as changes in TEC with solar activity, season, and LT, semiannual variation in TEC, and stronger enhancement in TEC in March as compared to October.

The new empirical model properly captures several features that are not well represented by IRI-2016, in particular wintertime TEC for moderate to high solar flux, and LT variations of TEC for low solar flux conditions. However, the largest strength of our model in comparison with IRI-2016 is an accurate description of TEC variation in response to short-term changes in solar flux.

Future efforts envision extension of the modeling approach to other longitudes and latitudes, as well as inspection and introduction of additional space weather and meteorological drivers.

7 Acknowledgements

L.P.G. and C. T. acknowledge support of this study from NASA grant 80NSSC19K0262. L. P. G., A. J. C., S. R. Z. and C. T. also acknowledge funding from the ONR Grant N00014-17-1-2186. C.T. gratefully acknowledges support from the US National Science Foundation (NSF) REU (Research Experience for Undergraduates) program grant AST-1659420 to the Massachusetts Institute of Technology (MIT) Haystack Observatory that funded his effort in summer 2019. TEC data processing and research activities at MIT Haystack

904 Observatory are supported by US NSF grant AGS-1952737. W. K. T. acknowledges sup-
 905 port from SPAWAR contract N6600120P6336 for the production of the S10, M10, and
 906 Y10 indices.

907 All of the data used in this paper are publicly available. GPS TEC data products
 908 and access through the CEDAR Madrigal distributed data system (<http://cedar.openmadrigal.org/>)
 909 are provided to the community by the MIT Haystack Observatory. The $F_{10.7}$ proxy
 910 and A_p3 index are also available from (<http://cedar.openmadrigal.org/>). The Mg
 911 II core-to-wing ratio is available at (<http://www.iup.uni-bremen.de/UVSAT/Datasets/mgii>).
 912 $S_{10.7}$ index data is provided by (<https://sol.spacenvironment.net/JP2008/>).
 913 $E_{10.7}$ index is provided by Space Environment Technologies (SET) (<http://www.spacewx.com/solar2000.html>). The SOHO SEM EUV data are made available by USC Dorn-
 914 sife (<https://dornsifecms.usc.edu/space-sciences-center/download-sem-data/>).
 915 The FISM2 EUV and Composite Lyman-alpha data are available from the LASP Inter-
 916 active Solar Irradiance Data Center (<http://lasp.colorado.edu/lisird/>). The TIMED
 917 SEE data are available from the University of Colorado at Boulder Laboratory for At-
 918 mospheric and Space Physics (LASP) website (<http://lasp.colorado.edu/home/see/data/>).
 920

921 Data for TEC processing is provided from the following organizations: UNAVCO,
 922 Scripps Orbit and Permanent Array Center, Institut Geographique National, France, In-
 923 ternational GNSS Service, The Crustal Dynamics Data Information System (CDDIS),
 924 National Geodetic Survey, Instituto Brasileiro de Geografia e Estatística, RAMSAC CORS
 925 of Instituto Geográfico Nacional de la República Argentina, Arecibo Observatory, Low-
 926 Latitude Ionospheric Sensor Network (LISN), Topcon Positioning Systems, Inc., Cana-
 927 dian High Arctic Ionospheric Network, Centro di Ricerche Sismologiche, Système d’Observation
 928 du Niveau des Eaux Littorales (SONEL), RENAG : REseau NATional GPS permanent,
 929 GeoNet - the official source of geological hazard information for New Zealand, GNSS Ref-
 930 erence Networks, Finnish Meteorological Institute, and SWEPOS - Sweden.

931 The authors acknowledge the MATLAB interface to IRI-2016 that was used in this
 932 study and available at <https://github.com/space-physics/IRI2016>.

933 References

- 934 Aa, E., Zhang, D., Ridley, A. J., Xiao, Z., & Hao, Y. (2012). A global model:
 935 Empirical orthogonal function analysis of total electron content 1999-2009
 936 data. *Journal of Geophysical Research: Space Physics*, *117*(A3). doi:
 937 10.1029/2011ja017238
- 938 Alcay, S., Oztan, G., & Selvi, H. (2017). Comparison of IRI_PLAS and IRI.2012
 939 model predictions with GPS-TEC measurements in different latitude regions.
 940 *Annals of Geophysics*, *60*(5). doi: 10.4401/ag-7311
- 941 Balan, N., Shiokawa, K., Otsuka, Y., Kikuchi, T., Vijaya Lekshmi, D., Kawamura,
 942 S., ... Bailey, G. (2010). A physical mechanism of positive ionospheric storms
 943 at low latitudes and midlatitudes. *Journal of Geophysical Research: Space*
 944 *Physics*, *115*(A2).
- 945 Banks, P., & Kockarts, G. (1973). Aeronomy - part a. *Academic Press, New York*
 946 *and London*.
- 947 Bilitza, D. (2004). A correction for the IRI topside electron density model based
 948 on Alouette/ISIS topside sounder data. *Advances in Space Research*, *33*(6),
 949 838–843. doi: 10.1016/j.asr.2003.07.009
- 950 Bilitza, D., Altadill, D., Truhlik, V., Shubin, V., Galkin, I., Reinisch, B., & Huang,
 951 X. (2017). International Reference Ionosphere 2016: From ionospheric cli-
 952 mate to real-time weather predictions. *Space Weather*, *15*(2), 418–429. doi:
 953 10.1002/2016sw001593
- 954 Bilitza, D., Altadill, D., Zhang, Y., Mertens, C., Truhlik, V., Richards, P., ...

- 955 Reinisch, B. (2014). The International Reference Ionosphere 2012 – a model of
 956 international collaboration. *Journal of Space Weather and Space Climate*, 4.
 957 doi: 10.1051/swsc/2014004
- 958 Bouya, Z., Terkildsen, M., & Neudegg, D. (2010). Regional GPS-based iono-
 959 spheric TEC model over Australia using Spherical Cap Harmonic Analysis.
 960 In *COSPAR Scientific Assembly 2010: 38th COSPAR Scientific Assembly*,
 961 *Bremen, Germany, 18-25 July 2010: Abstracts* (p. 4). COSPAR.
- 962 Bowman, B., Tobiska, W. K., Marcos, F., Huang, C., Lin, C., & Burke, W. (2008a).
 963 A new empirical thermospheric density model JB2008 using new solar and
 964 geomagnetic indices. *AIAA/AAS Astrodynamics Specialist Conference and*
 965 *Exhibit*. doi: 10.2514/6.2008-6438
- 966 Bowman, B. R., Tobiska, W. K., & Kendra, M. J. (2008b). The thermo-
 967 spheric semiannual density response to solar EUV heating. *Journal of*
 968 *Atmospheric and Solar-Terrestrial Physics*, 70(11-12), 1482–1496. doi:
 969 10.1016/j.jastp.2008.04.020
- 970 Brum, C. G. M., Rodrigues, F. D. S., Santos, P. T. D., Matta, A. C., Aponte, N.,
 971 Gonzalez, S. A., & Robles, E. (2011). A modeling study of fof2 and hmf2
 972 parameters measured by the Arecibo incoherent scatter radar and compar-
 973 ison with IRI model predictions for solar cycles 21, 22, and 23. *Journal of*
 974 *Geophysical Research: Space Physics*, 116(A3). doi: 10.1029/2010ja015727
- 975 Burns, A. G., Solomon, S. C., Wang, W., Qian, L., Zhang, Y., & Paxton, L. J.
 976 (2012). Daytime climatology of ionospheric NmF2 and hmf2 from COS-
 977 MIC data. *Journal of Geophysical Research: Space Physics*, 117(A9). doi:
 978 10.1029/2012ja017529
- 979 Chamberlin, P. C., Woods, T. N., & Eparvier, F. G. (2007, July). Flare Irradi-
 980 ance Spectral Model (FISM): Daily component algorithms and results. *Space*
 981 *Weather*, 5(7), S07005. doi: 10.1029/2007SW000316
- 982 Chamberlin, P. C., Woods, T. N., & Eparvier, F. G. (2008). Flare Irradiance Spec-
 983 tral Model (FISM): Flare component algorithms and results. *Space Weather*,
 984 6(5). doi: 10.1029/2007sw000372
- 985 Chen, Z., Zhang, S.-R., Coster, A. J., & Fang, G. (2015). EOF analysis and model-
 986 ing of GPS TEC climatology over North America. *Journal of Geophysical Re-*
 987 *search: Space Physics*, 120(4), 3118–3129. doi: 10.1002/2014ja020837
- 988 Cherniak, I., Zakharenkova, I., Krankowski, A., & Shagimuratov, I. (2012). Plasma-
 989 spheric electron content derived from GPS TEC and FORMOSAT-3/COSMIC
 990 measurements: Solar minimum condition. *Advances in Space Research*, 50(4),
 991 427–440. doi: 10.1016/j.asr.2012.04.002
- 992 Emmert, J. T., Picone, J. M., & Meier, R. R. (2008). Thermospheric global average
 993 density trends, 1967–2007, derived from orbits of 5000 near-earth objects. *Geo-*
 994 *physical Research Letters*, 35(5). doi: 10.1029/2007gl032809
- 995 Feng, J. F., Han, B., Zhao, Z., & Wang, Z. (2019). A new global total electron con-
 996 tent empirical model. *Remote Sensing*, 11, 706. doi: 10.3390/rs11060706
- 997 Fuller-Rowell, T. J. (1998). The “thermospheric spoon”: A mechanism for the
 998 semiannual density variation. *Journal of Geophysical Research: Space Physics*,
 999 103(A3), 3951–3956. doi: 10.1029/97ja03335
- 1000 Gu, S.-Y., Ruan, H., Yang, C.-Y., Gan, Q., Dou, X., & Wang, N. (2018). The
 1001 morphology of the 6-day wave in both the neutral atmosphere and f region
 1002 ionosphere under solar minimum conditions. *Journal of Geophysical Research:*
 1003 *Space Physics*, 123(5), 4232–4240. doi: 10.1029/2018ja025302
- 1004 Gulyaeva, T., Arikan, F., Sezen, U., & Poustovalova, L. (2018). Eight proxy indices
 1005 of solar activity for the international reference ionosphere and plasmasphere
 1006 model. *Journal of Atmospheric and Solar-Terrestrial Physics*, 172, 122–128.
 1007 doi: 10.1016/j.jastp.2018.03.025
- 1008 Habarulema, J. B., Mckinnell, L.-A., & Opperman, B. D. (2010). TEC measure-
 1009 ments and modelling over Southern Africa during magnetic storms; a compar-

- 1010 ative analysis. *Journal of Atmospheric and Solar-Terrestrial Physics*, 72(5-6),
1011 509–520. doi: 10.1016/j.jastp.2010.01.012
- 1012 Habarulema, J. B., Mckinnell, L.-A., & Opperman, B. D. L. (2011). Regional GPS
1013 TEC modeling; Attempted spatial and temporal extrapolation of TEC using
1014 neural networks. *Journal of Geophysical Research: Space Physics*, 116(A4).
1015 doi: 10.1029/2010ja016269
- 1016 He, C., Yang, Y., Carter, B., Kerr, E., Wu, S., Deleflie, F., . . . et al. (2018). Re-
1017 view and comparison of empirical thermospheric mass density models. *Progress*
1018 *in Aerospace Sciences*, 103, 31–51. doi: 10.1016/j.paerosci.2018.10.003
- 1019 Heath, D. F., & Schlesinger, B. M. (1986). The Mg 280-nm doublet as a moni-
1020 tor of changes in solar ultraviolet irradiance. *Journal of Geophysical Research*,
1021 91(D8), 8672–8682. doi: 10.1029/jd091id08p08672
- 1022 Huang, Z., & Yuan, H. (2014). Ionospheric single-station TEC short-term fore-
1023 cast using RBF neural network. *Radio Science*, 49(4), 283–292. doi: 10.1002/
1024 2013rs005247
- 1025 ISO14222. (2013). *Iso 14222: Space environment (natural and artificial) –*
1026 *earth upper atmosphere*. Retrieved from [https://www.iso.org/standard/](https://www.iso.org/standard/54507.html)
1027 54507.html
- 1028 ISO16457. (2014). *Iso 16457: Space systems – space environment (natural and*
1029 *artificial) – the earth’s ionosphere model: international reference iono-*
1030 *sphere (iri) model and extension to the plasmasphere*. Retrieved from
1031 <https://www.iso.org/standard/61556.html>
- 1032 Jacchia, L. G. (1959). Solar effects on the acceleration of artificial satellites. *SAO*
1033 *Special Report*, 29.
- 1034 Jakowski, N., Mayer, C., Hoque, M. M., & Wilken, V. (2011). Total electron content
1035 models and their use in ionosphere monitoring. *Radio Science*, 46(6). doi: 10
1036 .1029/2010rs004620
- 1037 Jones, M., Emmert, J. T., Drob, D. P., Picone, J. M., & Meier, R. R. (2018). Ori-
1038 gins of the thermosphere-ionosphere semiannual oscillation: Reformulating the
1039 “thermospheric spoon” mechanism. *Journal of Geophysical Research: Space*
1040 *Physics*, 123(1), 931–954. doi: 10.1002/2017ja024861
- 1041 Kim, D.-S., & Dong-Ku, S. (2011). *A standardization technique to reduce the prob-*
1042 *lem of multicollinearity in polynomial regression analysis*. Retrieved from
1043 http://stat.fi/isi99/proceedings/arkisto/varasto/kim_0574.pdf
- 1044 Komjathy, A., Sparks, L., Wilson, B. D., & Mannucci, A. J. (2005). Automated
1045 daily processing of more than 1000 ground-based gps receivers for studying
1046 intense ionospheric storms. *Radio Science*, 40(6). doi: 10.1029/2005rs003279
- 1047 Kumar, S. (2016). Performance of IRI-2012 model during a deep solar minimum
1048 and a maximum year over global equatorial regions. *Journal of Geophysical*
1049 *Research: Space Physics*, 121(6), 5664–5674. doi: 10.1002/2015ja022269
- 1050 Kumar, S., Tan, E. L., & Murti, D. S. (2015). Impacts of solar activity on per-
1051 formance of the IRI-2012 model predictions from low to mid latitudes. *Earth,*
1052 *Planets and Space*, 67(1). doi: 10.1186/s40623-015-0205-3
- 1053 Lean, J. L. (2019). One- to 10-day forecasts of ionospheric total electron con-
1054 tent using a statistical model. *Space Weather*, 17(2), 313–338. doi:
1055 10.1029/2018sw002077
- 1056 Lean, J. L., Meier, R. R., Picone, J. M., Sassi, F., Emmert, J. T., & Richards, P. G.
1057 (2016). Ionospheric total electron content: Spatial patterns of variability.
1058 *Journal of Geophysical Research: Space Physics*, 121(10), 10,367-10,402.
- 1059 Lean, J. L., Woods, T. N., Eparvier, F. G., Meier, R. R., Strickland, D. J., Correia,
1060 J. T., & Evans, J. S. (2011). Solar extreme ultraviolet irradiance: Present,
1061 past, and future. *Journal of Geophysical Research: Space Physics*, 116(A1).
1062 doi: 10.1029/2010ja015901
- 1063 Lei, J., Liu, L., Wan, W., & Zhang, S.-R. (2005). Variations of electron density
1064 based on long-term incoherent scatter radar and ionosonde measurements over

- 1065 Millstone Hill. *Radio Science*, 40(2). doi: 10.1029/2004rs003106
- 1066 Li, S., Li, L., & Peng, J. (2016). Variability of Ionospheric TEC and the Perform-
1067 mance of the IRI-2012 Model at the BJFS Station, China. *Acta Geophysica*,
1068 64(5), 1970–1987. doi: 10.1515/acgeo-2016-0075
- 1069 Liu, J., Chen, R., An, J., Wang, Z., & Hyyppä, J. (2014). Spherical cap harmonic
1070 analysis of the Arctic ionospheric TEC for one solar cycle. *Journal of Geophys-
1071 ical Research: Space Physics*, 119(1), 601–619. doi: 10.1002/2013ja019501
- 1072 Liu, J., Liu, L., Zhao, B., Wan, W., & Chen, Y. (2012). Empirical modeling of iono-
1073 spheric F2 layer critical frequency over Wakkanai under geomagnetic quiet and
1074 disturbed conditions. *Science China Technological Sciences*, 55(5), 1169–1177.
1075 doi: 10.1007/s11431-012-4801-1
- 1076 Liu, L., Wan, W., Ning, B., Pirog, O. M., & Kurkin, V. I. (2006). Solar activity
1077 variations of the ionospheric peak electron density. *Journal of Geophysical Re-
1078 search*, 111(A8). doi: 10.1029/2006ja011598
- 1079 Liu, L., Yao, Y., Kong, J., & Shan, L. (2018). Plasmaspheric Electron Content
1080 Inferred from Residuals between GNSS-Derived and TOPEX/JASON Vertical
1081 TEC Data. *Remote Sensing*, 10(4), 621. doi: 10.3390/rs10040621
- 1082 Lu, G., Goncharenko, L. P., Richmond, A., Roble, R., & Aponte, N. (2008). A day-
1083 side ionospheric positive storm phase driven by neutral winds. *Journal of Geo-
1084 physical Research: Space Physics*, 113(A8).
- 1085 Machol, J., Snow, M., Woodraska, D., Woods, T., Viereck, R., & Coddington, O.
1086 (2019). An improved lyman-alpha composite. *Earth and Space Science*, 6(12),
1087 2263–2272. doi: 10.1029/2019ea000648
- 1088 Mannucci, A. J., Wilson, B. D., Yuan, D. N., Ho, C. H., Lindqwister, U. J., &
1089 Runge, T. F. (1998). A global mapping technique for gps-derived ionospheric
1090 total electron content measurements. *Radio Science*, 33(3), 565–582. doi:
1091 10.1029/97rs02707
- 1092 Mao, T., Wan, W., Yue, X., Sun, L., Zhao, B., & Guo, J. (2008). An empirical or-
1093 thogonal function model of total electron content over China. *Radio Science*,
1094 43(2). doi: 10.1029/2007rs003629
- 1095 Mao, T., Wan, W.-X., & Liu, L.-B. (2005). An EOF based empirical model of TEC
1096 over Wuhan. *Chinese Journal of Geophysics*, 48(4), 827–834. doi: 10.1002/cjg2
1097 .720
- 1098 Maruyama, T. (2010). Solar proxies pertaining to empirical ionospheric total
1099 electron content models. *Journal of Geophysical Research: Space Physics*,
1100 115(A4). doi: 10.1029/2009ja014890
- 1101 Maruyama, T. (2011). Modified solar flux index for upper atmospheric applica-
1102 tions. *Journal of Geophysical Research: Space Physics*, 116(A8). doi: 10.1029/
1103 2010ja016322
- 1104 Mendillo, M. (2006). Storms in the ionosphere: Patterns and processes for total elec-
1105 tron content. *Reviews of Geophysics*, 44(4). doi: 10.1029/2005rg000193
- 1106 Mukhtarov, P., Andonov, B., & Pancheva, D. (2013a). Global empirical model of
1107 TEC response to geomagnetic activity. *Journal of Geophysical Research: Space
1108 Physics*, 118(10), 6666–6685. doi: 10.1002/jgra.50576
- 1109 Mukhtarov, P., Pancheva, D., Andonov, B., & Pashova, L. (2013b). Global
1110 TEC maps based on GNSS data: 1. Empirical background TEC model.
1111 *Journal of Geophysical Research: Space Physics*, 118(7), 4594–4608. doi:
1112 10.1002/jgra.50413
- 1113 Nava, B., Coisson, P., & Radicella, S. (2008). A new version of the NeQuick iono-
1114 sphere electron density model. *Journal of Atmospheric and Solar-Terrestrial
1115 Physics*, 70(15), 1856–1862. doi: 10.1016/j.jastp.2008.01.015
- 1116 Prölss, G. W. (1995). Ionospheric f-region storms. *Handbook of atmospheric electro-
1117 dynamics*, 2, 195–248.
- 1118 Qin, Y., Gu, S., Dou, X., Gong, Y., Chen, G., Zhang, S., & Wu, Q. (2019). Clima-
1119 tology of the Quasi-6-Day Wave in the Mesopause Region and Its Modulations

- 1120 on Total Electron Content During 2003–2017. *Journal of Geophysical Research:*
 1121 *Space Physics*, 124(1), 573–583. doi: 10.1029/2018ja025981
- 1122 Richards, P. G. (2001). Seasonal and solar cycle variations of the ionospheric
 1123 peak electron density: Comparison of measurement and models. *Jour-*
 1124 *nal of Geophysical Research: Space Physics*, 106(A7), 12803–12819. doi:
 1125 10.1029/2000ja000365
- 1126 Richards, P. G., Fennelly, J. A., & Torr, D. G. (1994). EUVAC: A solar EUV Flux
 1127 Model for aeronomic calculations. *Journal of Geophysical Research*, 99(A5),
 1128 8981. doi: 10.1029/94ja00518
- 1129 Rideout, W., & Coster, A. (2006). Automated gps processing for global total elec-
 1130 tron content data. *GPS Solutions*, 10(3), 219–228. doi: 10.1007/s10291-006
 1131 -0029-5
- 1132 Rishbeth, H., Müller-Wodarg, I. C. F., Zou, L., Fuller-Rowell, T. J., Millward, G. H.,
 1133 Moffett, R. J., & et al. (2000). Annual and semiannual variations in the iono-
 1134 spheric F2-layer: II. Physical discussion. *Annales Geophysicae*, 18(8), 945–956.
 1135 doi: 10.1007/s00585-000-0945-6
- 1136 Scherliess, L., Tzagouri, I., Yizengaw, E., Bruinsma, S., Shim, J. S., Coster, A.,
 1137 & Retterer, J. M. (2019). The international community coordinated mod-
 1138 eling center space weather modeling capabilities assessment: Overview of
 1139 ionosphere/thermosphere activities. *Space Weather*, 17(4), 527–538. doi:
 1140 10.1029/2018sw002036
- 1141 Schonfeld, S. J., White, S. M., Henney, C. J., Hock-Mysliwiec, R. A., & Mcateer,
 1142 R. T. J. (2019). The Slowly Varying Corona. II. The Components of F 10.7
 1143 and Their Use in EUV Proxies. *The Astrophysical Journal*, 884(2), 141. doi:
 1144 10.3847/1538-4357/ab3af9
- 1145 Schunk, R. W., & Nagy, A. F. (2009). *Ionospheres: physics, plasma physics, and*
 1146 *chemistry* (2nd ed.). Cambridge Univ. Press.
- 1147 Shim, J. S., Jee, G., & Scherliess, L. (2017a). Climatology of plasmaspheric to-
 1148 tal electron content obtained from Jason 1 satellite. *Journal of Geophysical Re-*
 1149 *search: Space Physics*, 122(2), 1611–1623. doi: 10.1002/2016ja023444
- 1150 Shim, J. S., Kuznetsova, M., Rastätter, L., Bilitza, D., Butala, M., Codrescu, M.,
 1151 ... et al. (2012). CEDAR Electrodynamics Thermosphere Ionosphere (ETI)
 1152 challenge for systematic assessment of ionosphere/thermosphere models: Elec-
 1153 tron density, neutral density, NmF2, and hmF2 using space based observations.
 1154 *Space Weather*, 10(10). doi: 10.1029/2012sw000851
- 1155 Shim, J. S., Kuznetsova, M., Rastätter, L., Hesse, M., Bilitza, D., Butala, M., & et
 1156 al. (2011). CEDAR Electrodynamics Thermosphere Ionosphere (ETI) Chal-
 1157 lenge for systematic assessment of ionosphere/thermosphere models: NmF2,
 1158 hmF2, and vertical drift using ground-based observations. *Space Weather*,
 1159 9(12). doi: 10.1029/2011sw000727
- 1160 Shim, J. S., Rastätter, L., Kuznetsova, M., Bilitza, D., Codrescu, M., Coster, A. J.,
 1161 ... et al. (2017b). CEDAR-GEM challenge for systematic assessment of iono-
 1162 sphere/thermosphere models in predicting TEC during the 2006 December
 1163 storm event. *Space Weather*, 15(10), 1238–1256. doi: 10.1002/2017sw001649
- 1164 Shim, J. S., Tzagouri, I., Goncharenko, L., Rastaetter, L., Kuznetsova, M., Bilitza,
 1165 D., ... et al. (2018). Validation of ionospheric specifications during geo-
 1166 magnetic storms: TEC and foF2 during the 2013 March storm event. *Space*
 1167 *Weather*, 16(11), 1686–1701. doi: 10.1029/2018sw002034
- 1168 Tariku, Y. A. (2016). The study of variability of TEC over mid-latitude American
 1169 regions during the ascending phase of solar cycle 24 (2009–2011). *Advances in*
 1170 *Space Research*, 58(4), 598–608. doi: 10.1016/j.asr.2016.05.012
- 1171 Tariku, Y. A. (2019). Mid latitude ionospheric TEC modeling and the IRI model
 1172 validation during the recent high solar activity (2013–2015). *Advances in Space*
 1173 *Research*, 63(12), 4025–4038. doi: 10.1016/j.asr.2019.03.010
- 1174 Themens, D. R., Jayachandran, P. T., Galkin, I., & Hall, C. (2017). The Empirical

- 1175 Canadian High Arctic Ionospheric Model (E-CHAIM): NmF2 and hmF2. *Journal of Geophysical Research: Space Physics*, 122(8), 9015–9031. doi: 10.1002/
- 1176 2017ja024398
- 1177
- 1178 Thomas, E., Baker, J., Ruohoniemi, J., Coster, A., & Zhang, S.-R. (2016). The
- 1179 geomagnetic storm time response of gps total electron content in the north
- 1180 american sector. *Journal of Geophysical Research: Space Physics*, 121(2),
- 1181 1744–1759.
- 1182 Tobiska, W., & Bouwer, S. (2005). Solar flare evolution model for operational users.
- 1183 In J. Goodman (Ed.), *2005 ionospheric effects symposium* (p. 76–76). JMG
- 1184 Associates.
- 1185 Tobiska, W. K. (2002). E10.7 use for global atmospheric density forecasting in 2001.
- 1186 *AIAA/AAS Astrodynamics Specialist Conference and Exhibit*. doi: 10.2514/6.
- 1187 .2002-4892
- 1188 Tobiska, W. K., Bouwer, S. D., & Bowman, B. R. (2008). The development
- 1189 of new solar indices for use in thermospheric density modeling. *Journal of Atmospheric and Solar-Terrestrial Physics*, 70(5), 803–819. doi:
- 1190 10.1016/j.jastp.2007.11.001
- 1191
- 1192 Vergados, P., Komjathy, A., Runge, T. F., Butala, M. D., & Mannucci, A. J. (2016).
- 1193 Characterization of the impact of glonass observables on receiver bias es-
- 1194 timation for ionospheric studies. *Radio Science*, 51(7), 1010–1021. doi:
- 1195 10.1002/2015rs005831
- 1196 Viereck, R., Puga, L., McMullin, D., Judge, D., Weber, M., & Tobiska, W. K.
- 1197 (2001). The Mg II index: A proxy for solar EUV. *Geophysical Research*
- 1198 *Letters*, 28(7), 1343–1346. doi: 10.1029/2000gl012551
- 1199 Vierinen, J., Coster, A. J., Rideout, W. C., Erickson, P. J., & Norberg, J. (2016).
- 1200 Statistical framework for estimating GNSS bias. *Atmospheric Measurement*
- 1201 *Techniques*, 9(3), 1303–1312. doi: 10.5194/amt-9-1303-2016
- 1202 Wieman, S., Didkovsky, L., & Judge, D. (2014). Resolving differences in absolute ir-
- 1203 radiance measurements between the soho/celias/sem and the sdo/eve. In *Coro-*
- 1204 *nal magnetometry* (pp. 285–303). Springer.
- 1205 Wood, B. E., Lean, J. L., McDonald, S. E., & Wang, Y.-M. (2016). Compara-
- 1206 tive ionospheric impacts and solar origins of nine strong geomagnetic storms
- 1207 in 2010–2015. *Journal of Geophysical Research: Space Physics*, 121(6),
- 1208 4938–4965. doi: 10.1002/2015ja021953
- 1209 Woods, T., Bailey, S., Eparvier, F., Lawrence, G., Lean, J., McClintock, B., & et
- 1210 al. (2000). TIMED solar EUV experiment. *Physics and Chemistry of the*
- 1211 *Earth, Part C: Solar, Terrestrial & Planetary Science*, 25(5-6), 393–396. doi:
- 1212 10.1016/s1464-1917(00)00040-4
- 1213 Woods, T. N. (2005). Solar EUV Experiment (SEE): Mission overview and first re-
- 1214 sults. *Journal of Geophysical Research*, 110(A1). doi: 10.1029/2004ja010765
- 1215 Yamazaki, Y., Stolle, C., Matzka, J., & Alken, P. (2018). Quasi-6-day wave mod-
- 1216 ulation of the equatorial electrojet. *Journal of Geophysical Research: Space*
- 1217 *Physics*, 123(5), 4094–4109. doi: 10.1029/2018ja025365
- 1218 Yizengaw, E., Moldwin, M., Galvan, D., Iijima, B., Komjathy, A., & Mannucci, A.
- 1219 (2008). Global plasmaspheric TEC and its relative contribution to GPS TEC.
- 1220 *Journal of Atmospheric and Solar-Terrestrial Physics*, 70(11-12), 1541–1548.
- 1221 doi: 10.1016/j.jastp.2008.04.022
- 1222 Zakharenkova, I., Cherniak, I., Krankowski, A., & Shagimuratov, I. (2015). Vertical
- 1223 tec representation by IRI 2012 and IRI Plas models for European midlatitudes.
- 1224 *Advances in Space Research*, 55(8), 2070–2076. doi: 10.1016/j.asr.2014.07.027
- 1225 Zhang, S.-R., Holt, J. M., Erickson, P. J., & Goncharenko, L. P. (2015, May). Day-
- 1226 to-day variability and solar preconditioning of thermospheric temperature
- 1227 over Millstone Hill. *Journal of Geophysical Research: Space Physics*, 120(5),
- 1228 3913–3927.
- 1229 Zhang, S.-R., Holt, J. M., van Eyken, A. P., McCready, M., Amory-Mazaudier, C.,

1230 Fukao, S., & Sulzer, M. P. (2005). Ionospheric local model and climatology
1231 from long-term databases of multiple incoherent scatter radars. *Geophysical*
1232 *Research Letters*, *32*(20), 9481.